Moored Turbulence Measurements Using Pulse-Coherent Doppler Sonar

SETH F. ZIPPEL,[a] J. THOMAS FARRAR,[a] CHRISTOPHER J. ZAPPA,[b] UNA MILLER,[b] LOUIS ST. LAURENT,[c] TAKASHI IJICHI,[d] ROBERT A. WELLER,[a] LEAH MCRAVEN,[a] SVEN NYLUND,[e] AND DEBORAH LE BEL[f]

[a] *Woods Hole Oceanographic Institution, Woods Hole, Massachusetts*
[b] *Lamont-Doherty Earth Observatory, Columbia University, Palisades, New York*
[c] *Applied Physics Laboratory, University of Washington, Seattle, Washington*
[d] *Department of Earth and Planetary Science, The University of Tokyo, Tokyo, Japan*
[e] *Nortek Group, Rud, Norway*
[f] *Gulf of Mexico Research Initiative Information and Data Cooperative, Texas A&M University–Corpus Christi, Corpus Christi, Texas*

(Manuscript received 12 January 2021, in final form 28 June 2021)

ABSTRACT: Upper-ocean turbulence is central to the exchanges of heat, momentum, and gases across the air–sea interface and therefore plays a large role in weather and climate. Current understanding of upper-ocean mixing is lacking, often leading models to misrepresent mixed layer depths and sea surface temperature. In part, progress has been limited by the difficulty of measuring turbulence from fixed moorings that can simultaneously measure surface fluxes and upper-ocean stratification over long time periods. Here we introduce a direct wavenumber method for measuring turbulent kinetic energy (TKE) dissipation rates ϵ from long-enduring moorings using pulse-coherent ADCPs. We discuss optimal programming of the ADCPs, a robust mechanical design for use on a mooring to maximize data return, and data processing techniques including phase-ambiguity unwrapping, spectral analysis, and a correction for instrument response. The method was used in the Salinity Processes Upper-Ocean Regional Study (SPURS) to collect two year-long datasets. We find that the mooring-derived TKE dissipation rates compare favorably to estimates made nearby from a microstructure shear probe mounted to a glider during its two separate 2-week missions for $O(10^{-8}) \leq \epsilon \leq O(10^{-5})$ $m^2 s^{-3}$. Periods of disagreement between turbulence estimates from the two platforms coincide with differences in vertical temperature profiles, which may indicate that barrier layers can substantially modulate upper-ocean turbulence over horizontal scales of 1–10 km. We also find that dissipation estimates from two different moorings at 12.5 and at 7 m are in agreement with the surface buoyancy flux during periods of strong nighttime convection, consistent with classic boundary layer theory.

SIGNIFICANCE STATEMENT: This study outlines a method to estimate ocean turbulence from long-enduring platforms. It is difficult to make this measurement using commonly accepted turbulence estimation methods because of ocean waves, platform motions, battery and data limitations, biofouling, and the fragility of some common turbulence instruments. We applied the method at three sites and compared the results from the new method with those from short-duration datasets that use a currently accepted method. We outline the range and limitations of the new method, based both on the instrument's principles of operation and on the comparison with an established method. Our intention is that the new method may be applied by others in future long-enduring deployments, which will increase the number of available turbulence datasets in the upper ocean.

KEYWORDS: Ocean; Turbulence; Atmosphere-ocean interaction; Boundary layer; Oceanic mixed layer; In situ oceanic observations

1. Introduction

Upper-ocean turbulence modifies air–sea fluxes of momentum, heat, and gases that are important for climate and weather prediction. Ocean turbulence is also important for understanding the transport of buoyant material such as biota and plastics. Of particular interest in the upper ocean are measurements of TKE dissipation rate ϵ, which characterizes the smallest scales of motion. Dissipation rates are challenging to measure directly, as they depend on velocity gradients at very small scales (typically less than millimeter scale). Pope (2000) summarized decades of theory and laboratory studies (Kolmogorov 1941; von Kármán 1948; Comte-Bellot and Corrsin 1971; Saddoughi and Veeravalli 1994; and many others) with a form for the radial wavenumber spectrum of turbulent velocity,

$$E(\kappa) = c\epsilon^{2/3}\kappa^{-5/3} f_L(\kappa L) f_\eta(\kappa\eta), \quad (1)$$

where c is a constant, ϵ is the TKE dissipation rate, κ is the radial wavenumber, and f_L and f_η are shape functions to describe the energy containing, and dissipative scales, respectively [Pope 2000, Eq. (6.246) therein]. Here, we follow the notation used in Pope (2000) such that $\kappa^2 = k_1^2 + k_2^2 + k_3^2$, where k_1, k_2,

Denotes content that is immediately available upon publication as open access.

Corresponding author: Seth F. Zippel, szippel@whoi.edu

DOI: 10.1175/JTECH-D-21-0005.1

© 2021 American Meteorological Society. For information regarding reuse of this content and general copyright information, consult the AMS Copyright Policy (www.ametsoc.org/PUBSReuseLicenses).

Brought to you by NOAA Central Library | Unauthenticated | Downloaded 11/30/21 04:35 PM UTC

and k_3 are the wavenumbers in the along-flow, cross-flow, and vertical directions, and L represents the longest scales of turbulent motion that contain the majority of turbulent kinetic energy for scales $\kappa L \sim 1$ and smaller. Similarly, η represents the Kolmogorov length scale, the scale at which viscous effects turn kinetic energy to heat in the dissipative range ($\kappa\eta \sim 1$ and larger).

The most commonly accepted method, or "gold standard," for estimating TKE dissipation rates in the ocean is through microstructure shear measurements. These methods use airfoil shear probes to sense the difference in velocity fluctuations at very high frequency f, which is converted to wavenumber using the fall speed U of the probe and Taylor's frozen field hypothesis, $k_1 = 2\pi f/U$. These spectra are compared with a shear spectrum, which can be derived from a universal TKE spectrum (Oakey 1982). Many different shape functions $f_\eta(\kappa\eta)$ have been proposed; however, it is standard to fit a heuristic spectrum derived from measurements (Nasmyth 1970), which are presented in tabular form in Oakey (1982) and presented as a functional fit to the tabular data in Wolk et al. (2002, appendix). This method is generally considered the most direct method of estimating TKE dissipation rates, as it resolves motions at or near the dissipative scales ($\kappa\eta \sim 1$). This measurement technique can be expensive and difficult to use on long-duration moorings due to the sensitivity of the airfoil probes to damage, and the need for a clean and constant advective velocity. Although there has been some success with using shear probes on moorings (Lueck et al. 1997), it has not become common practice.

The development of the χpod (Moum and Nash 2009), which derives turbulent statistics from measurements of temperature microstructure, has allowed for the inference of TKE dissipation rates from moorings. Similar to microstructure shear, this estimate relies on Taylor's frozen field hypothesis to convert measured frequency spectra into wavenumber spectra. In addition, this method assumes the eddy diffusivity of heat K_t and density K_ρ are equivalent, and following the method of Osborn (1980), uses a constant mixing efficiency parameter Γ and the local buoyancy frequency N^2 to estimate TKE dissipation rate through $K_\rho = \Gamma\epsilon/N^2$, where mixing efficiency parameter is $\Gamma = R_f/(1 - R_f)$ and R_f is the flux Richardson number. This relation between K_ρ, ϵ, and N^2 stems from an assumed TKE equation: $P + B = \epsilon$, with the flux Richardson number defined as $R_f = B/P$, with P being the production of turbulence by velocity shear and B being the buoyancy flux. This method has been effective in measuring turbulence from moorings (Zhang and Moum 2010; Perlin and Moum 2012; Smyth and Moum 2013), but the assumptions used in the (Osborn 1980; Osborn and Cox 1972; Oakey 1982) relation make it challenging to measure non-shear-driven turbulence. For example, pure buoyancy-driven convection precludes the use of the (Osborn 1980) relation, since this would cause a TKE equation to become $B = \epsilon$ and R_f, and by association Γ would be undefined. Further, recent studies (Scully et al. 2016; Fisher et al. 2018) have suggested wave-driven fluxes in the near-surface layer result from the pressure-velocity correlation in the turbulent transport term, which is not included in (Osborn 1980) TKE balance. Last, the assumption of Taylor's frozen field hypothesis is not always valid. Strong wave orbital motions make the frozen field assumption challenging to apply, because aliasing can occur when converting from a frequency spectrum to a wavenumber spectrum (Lumley and Terray 1983). In the absence of waves, experimental studies have shown Taylor's hypothesis to fail in free shear flows (e.g., Tong and Warhaft 1995), which can occur when turbulence intensity is large in comparison with the mean flow.

Recently, acoustic Doppler current profilers (ADCPs) have seen use in estimating TKE dissipation rates from fixed platforms in coastal waters (Gargett 1994; Wiles et al. 2006) and near the ocean surface from moving platforms (Gemmrich 2010; Thomson 2012; Sutherland and Melville 2015; Zippel et al. 2020). ADCPs yield estimates of water velocity in a discretized profile, allowing for direct spatial estimates of turbulence that do not rely on Taylor's frozen field hypothesis. This spatial method is particularly important when estimating turbulence in the presence of surface gravity waves, as energetic wave orbital motions can obscure turbulent velocities in similar frequency ranges but tend to be more easily separated spatially. So far, these methods have primarily focused on using second-order structure functions over short distances near the surface where dissipation rates are large $\epsilon > 10^{-5}\,\mathrm{m^2\,s^3}$. Here, we discuss a wavenumber inertial subrange method intended for upper-ocean dissipation rates that are much smaller than those seen at the surface.

The inertial subrange commonly exists at scales larger than the dissipative scales, but below the largest turbulent scales (i.e., wavenumbers $1/L < \kappa < 1/\eta$), where the shape functions $f_L(\kappa L)$ and $f_\eta(\kappa\eta)$ are near 1 and the one-dimensional wavenumber spectrum is well described by the wavenumber and dissipation rate only,

$$E_{11}(k_1) = C_1\epsilon^{2/3}k_1^{-5/3}, \tag{2}$$

with $C_1 = 0.53$ (Sreenivasan 1995), and with the relation between the radial spectrum [Eq. (1)] and the 1D spectrum [Eq. (2)] described by Pope [2000, Eq. (6.216) therein]. Here, we present a wavenumber method for estimating TKE dissipation rate using an inertial subrange technique on data from pulse-coherent Doppler velocity profilers deployed on long duration moorings. In section 2, we overview the field programs, instrumentation, guidance on instrument setup, the mechanical deployment of the instrument on moorings, and a data processing workflow. Results from the method are compared with nearby microstructure data and surface fluxes in in section 3 and discussed in section 4. A summary of the results is presented in section 5.

2. Methods

Nortek Aquadopp 1- and 2-MHz pulse-coherent (HR) ADCPs were deployed at multiple depths on three surface moorings for approximately one year. Each Aquadopp was configured to sample a single beam in the horizontal plane. Sampling a single beam at higher sample rate was preferable to multiple beams at lower sample rate for directional consistency

Brought to you by NOAA Central Library | Unauthenticated | Downloaded 11/30/21 04:35 PM UTC

in the processing and analysis for each returned measurement. The sampled beam was oriented away from the mooring line (upflow direction) by a directional vane. The instruments were set to record data in 135 s bursts at the top of each hour, and then remain dormant for the remainder of the hour to conserve battery (Table 1). This results in 1080 profiles each hour for the 2-MHz instrument and 540 profiles each hour for the 1-MHz instrument. Using extended instrument housings with lithium batteries with this configuration, the instruments were able to sample hourly for a full year. These moorings, the ninth annual deployment of the Stratus Ocean Reference Station mooring (hereinafter Stratus 9 mooring; Weller 2015), the Salinity Processes Upper-Ocean Regional Study 1 (SPURS-1) central mooring (Farrar et al. 2015), and SPURS-2 central mooring (Farrar and Plueddemann 2019) are described briefly below. All three moorings were in 4000–5000 m of water, with an inverse catenary design. The moorings all had a 2.8-m surface buoy carrying surface meteorological instrumentation, chain in the upper few tens of meters, wire rope to about 1700 m, and synthetic rope below that depth.

The Stratus 9 mooring was deployed in the eastern tropical Pacific Ocean in October 2008 at 19°42′S, 85°35′W. It was recovered in January 2010. The mooring had a surface buoy equipped to observe surface meteorological conditions and support computation of the air–sea fluxes using bulk formulas methods. Along the mooring line, Sea-Bird 39 and Sea-Bird 37 instruments recorded temperature and conductivity, and mean currents were observed with vector-measuring current meters (VMCMs) and an RDI ADCP.

The SPURS-1 mooring was deployed in the North Atlantic subtropical gyre at 24°N, 38°W, from late 2012 to late 2013. The mooring was equipped with a surface flux buoy that measured a suite of meteorological parameters above and at the sea surface that can be used to estimate the fluxes of heat, momentum, and freshwater into the ocean surface (Fairall et al. 2003; Edson et al. 2013). These measurements included air temperature, humidity, wind speed, barometric pressure, precipitation, solar radiation (long and short wave), sea surface temperature, and sea surface salinity. Below the mooring was a densely instrumented mooring chain with conductivity and temperature measurements every 3 m for the upper 25 m, getting coarser with increasing depth (every 5 m from 25 to 90 m, and every 20 m from 110 to 160 m). Pulse-coherent ADCPs were deployed at 12.5-, 21.5-, 41.5-, 61.7-, 82-, 101.6-, and 121.6-m depths to make estimates of TKE dissipation rates, as described in this study. The mooring data were complemented by a large number of nearby autonomous assets, including two 12-day deployments of a Slocum glider with associated temperature and microstructure shear data (Bogdanoff 2017; St. Laurent and Merrifield 2017).

The SPURS-2 mooring was deployed at 10°N, 125°W, at the edge of the tropical eastern Pacific fresh pool with a buoy and mooring chain equipped similarly to the SPURS-1 mooring. The mooring estimated surface fluxes with the Improved Meteorological Packages (IMET) system, and had a chain of conductivity–temperature (CT) sensors densely spaced in the upper 100 m. On this mooring, five pulse-coherent ADCPs were placed at 7-, 21.5-, 41.5-, 61.7-, and 100-m water depth. Of these, the 61.7- and 100-m ADCPs failed, although limited data were able to be recovered from the 61.7-m instrument after recovery.

TABLE 1. Instrument configuration parameters, and their calculated range of measured TKE dissipation rates. Instruments measured one burst per hour for one year each.

Parameter	2 MHz	1 MHz
Pulse distance	2.22[a] m	3.33[a] m
Wrapping velocity V_r	0.063 m s^{-1}	0.085 m s^{-1}
Transmit pulse length	0.036 m	0.048 m
Receive gate width	0.034[a] m	0.044[a] m
User-programmed cell size	0.03[a] m	0.04[a] m
Blanking distance	0.096 m	0.189 m
No. of bins (cells)	63	70
Sample rate	8 Hz	4 Hz
No. of pings per sample N_p	10	13
Samples per burst	1080	540
Burst interval	3600 s	3600 s
Upper bound ϵ (wrapping)	10^{-5} m^2 s^{-3}	10^{-5} m^2 s^{-3}
Lower bound ϵ (correlation)	10^{-8}–10^{-9} m^2 s^{-3}	10^{-8}–10^{-9} m^2 s^{-3}

[a] The user-programmed value of cell size and pulse distance is automatically adjusted in Nortek software for a slant-beam projection and varies from the physical along-beam distances. Here, cell size varies from the receive gate width by this value, and the reported pulse distance are shown as the along-beam distances. The slant-beam offsets result in distances larger than the user programmed values by ~10%.

The methods described in this paper will be applied to all moorings. However, the focus is primarily on the SPURS-1 mooring data, which can be compared with microstructure-shear-derived estimates of TKE dissipation rate from the two 12-day glider deployments. The Stratus 9 mooring was an integral part of the evolution of the mechanical mount (to be discussed in section 2c); however, the processed dissipation rate data from the Stratus 9 mooring will be presented in a subsequent paper.

a. *Pulse-coherent ADCPs*

Pulse-coherent Doppler velocity profilers measure water velocity at a fine scale over a range of discretized locations. The measurement technique capitalizes on the relation between acoustic wave phase and the distance to the target that scatters the transmitted pulse. The change in phase with time can then be used to estimate local water velocity. Specifically, two acoustic pulses separated by time lag τ are used to determine the time rate of change of phase, which is related to the velocity as

$$V = \frac{1}{2\pi}\frac{\lambda}{2}\frac{\phi}{\tau}, \tag{3}$$

where V is the estimated velocity, $\lambda = C/F_0$ is the acoustic wavelength equivalent to the speed of sound in water divided by the system frequency, and ϕ is the measured phase between

Brought to you by NOAA Central Library | Unauthenticated | Downloaded 11/30/21 04:35 PM UTC

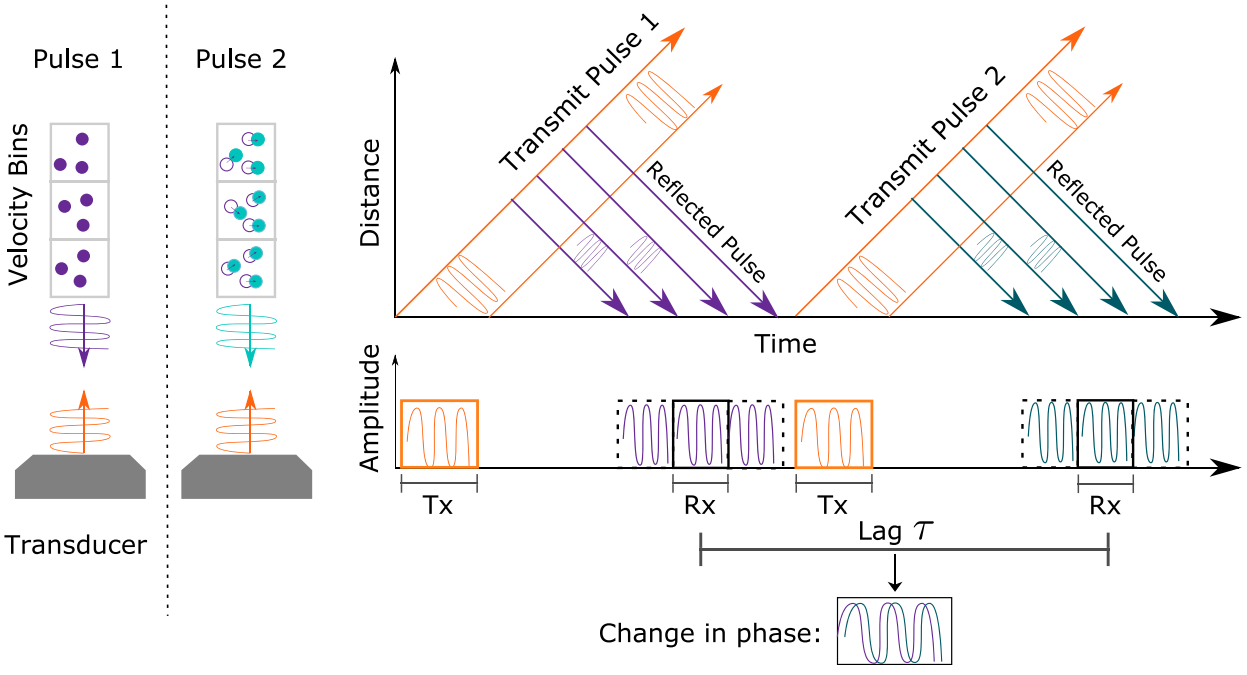

FIG. 1. A schematic demonstrating the pulse-coherent method. The acoustic transducer transmits pressure waves (Tx) into the water, which are scattered off moving particulate. Scattered sound travels back to the transducer, which samples the reflected signal using discrete range gates (Rx) in time. Two pulses are transmitted separated by time lag τ, and the change in phase between received pulses at lag τ is used to estimate the water velocity through Eq. (3). The schematic on the left shows sets of particles sampled by the first pulse (solid purple circles) and the same particles after time lag τ (cyan circles) that have been moved by the local water velocity. The two schematized axes on the right show a distance–time representation of the transmitted and reflected sound pulsesat the top and a representation of the amplitude time series seen by the transducer at the bottom.

the pulse pairs (Zedel et al. 1996; Veron and Melville 1999). A schematic of the pulse-pair matching is shown in Fig. 1.

While this technique allows for measurement of much smaller velocity fluctuations when compared with single-pulse autocorrelation (narrow- and broadband) methods, it is limited in the range of measured velocity as the phase is measured on the interval $-\pi \le \phi \le \pi$. Therefore, there is a limited measured velocity range set by a wrapping velocity V_r, which is related to the acoustic wavelength and the pulse lag,

$$V_r = \frac{C}{4F_0\tau}. \tag{4}$$

As such, these instruments are typically recommended for low energy environments where the range of velocities are expected to be small, and thus phase wrapping would not be an issue. The Nortek software expresses the lag τ in terms of pulse distance ℓ, which is determined using the speed of sound $\ell = C\tau/2$.

1) INSTRUMENT SAMPLING

As schematized in Fig. 1 the Nortek pulse-coherent Aquadopp uses near-rectangular transmit and receive windows in the pulse-to-pulse sampling scheme, meaning that the amplitude of the transmitted pulse rises abruptly from zero to a constant amplitude, and shuts off suddenly. In practice, each receive window is composed of a discrete number of subsamples M, related to the number of processor clock cycles occurring during the transmit or receive window. The available instrument bandwidth, however, is set by the duration of the monochromatic transmit pulse, which is matched to the receive window. That is, the instrument bandwidth is modified by the user-specified cell size, which determines the receive window duration. The instrument can be configured to average multiple ping pairs in time such that the reported velocity in a given range cell consists of N_p averaged pings, where each ping is derived from M subsamples.

The near-rectangular transmit and receive windows result in a spatial sampling filter, which can be treated as the convolution of a continuous velocity signal with two rectangular windows, $\tilde{V}(x) = V(x)T(L_T)R(L_R)$, where here $\tilde{V}(x)$ is the measured velocity, $V(x)$ is the true velocity signal, x is the along-beam coordinate direction, $T(L_T)$ and $R(L_R)$ are the transmit and receive windows, and L_T and L_R are the length of the transmit and receive windows. From the convolution theorem, the power spectral density of measured velocities will be affected by the sampling scheme as

$$|F\{\tilde{V}(x)\}|^2 = G(k_1, L_T, L_R)|F\{V(x)\}|^2, \tag{5}$$

where $F\{\}$ represents a Fourier transform and $G(k_1, L_T, L_R)$ is the power spectrum of two rectangular windows of length L_T

Brought to you by NOAA Central Library | Unauthenticated | Downloaded 11/30/21 04:35 PM UTC

and L_R. The Fourier transform of a single rectangular window is $F\{T(L_T)\} = \text{sinc}[k_1 L_t/(2\pi)]$, and the effect of two such windows (resulting in time-domain triangular/trapezoidal windows) results in an instrument transfer function,

$$G(k_1, L_T, L_R) = \text{sinc}\left(\frac{k_1 L_T}{2\pi}\right)^2 \text{sinc}\left(\frac{k_1 L_R}{2\pi}\right)^2. \quad (6)$$

In practice, the above instrument response function is an approximation because the instrument's transmit and receive windows are unlikely to be perfectly rectangular windows.

Here, we demonstrate these sampling effects using synthetic data, and show the degree to which the sampling spectral effects can be corrected by applying the inverse instrument transfer function. Multiple time series are synthesized to have a spectral shape consistent with an inertial subrange (a $k_1^{-5/3}$ power-law slope). White noise is added to the original time series, which is then used to create a "subsampled" time series by taking a sample every 10 data points in the original time series. A second "synthetically sampled" time series is made by first taking the convolution of a trapezoidal averaging window (consistent with a convolution of two rectangular windows) with the original time series, and then subsampling the convolved signal to simulate the sampling by the Aquadopp instrument. This process is repeated, and power spectra of the generated, uniformly subsampled, and synthetically sampled signals are averaged to increase statistical stability of the spectral estimates. The averaged power spectra of the two sampled time series are then compared with the original, as shown in Fig. 2. The power spectrum from the uniformly subsampled time series exhibits higher energy levels than the original signal with added noise, as subsampling (alone) raises the high-frequency end of the original spectrum due to aliasing. The simulation of Aquadopp sampling due to the effective spatial smoothing that acts to reduce energy in the tail below both the original signal and the uniformly subsampled case. A corrected spectrum is also shown in the figure, where the power spectrum of the synthetically sampled data is divided by the theoretical transfer function [Eq. (6)]. The corrected spectrum matches the spectrum made from the original signal to higher wavenumber than the uncorrected, and uniform subsample spectra. Because the sinc functions become small at high wavenumber and the synthetically sampled time series has some amount of increased variance due to aliasing from downsampling, the corrected spectrum becomes artificially large near the Nyquist wavenumber.

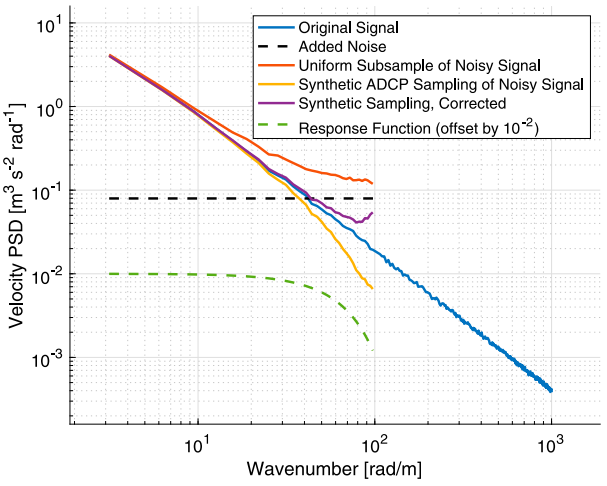

FIG. 2. Synthetic data created to have a power spectrum of the form $k^{-5/3}$ were sampled with a uniform subsample (orange) and with a double rectangular filter that mimics the sampling from an ADCP (yellow). White noise is added during both of the synthetic sampling procedures (dashed black), and the power spectrum of the sampled synthetic data is compared with the spectrum from the original synthetic time series (blue). The corrected, synthetically sampled spectrum (purple) fits the original signal over a much larger wavenumber range. The convolution filter described in Eq. (6) is shown in dashed green, offset for clarity.

2) NOISE ESTIMATION

The probability density function of pulse-pair estimates has been explored in the literature for radar methods (Miller and Rochwarger 1972), applied for the Doppler sonar case for relating sample correlations to velocity variance theoretically (Dillon et al. 2012), and tested with data (Shcherbina et al. 2018). These studies have shown that the variance of a velocity estimated from pulse-pair methods can be approximated as

$$\text{var}(V) = \frac{1}{N_p}\left(\frac{V_r}{\pi}\right)^2 \text{var}(\phi) \approx \left(\frac{V_r}{\pi}\right)^2 \frac{\hat{R}^{-2} - 1}{2N_p}, \quad (7)$$

where here $\hat{R}$ is the sample correlation coefficient and N_p is the number of averaged pings. Equation (7) differs slightly from that presented in Shcherbina et al. (2018) due to differences between the Aquadopp and the Signature1000 instruments. For the Aquadopp, the instrument bandwidth is limited by the transmit pulse length L_T, which is matched to the receive length L_R (or cell size), such that larger cells will contain more subsamples (or clock cycles), but these subsamples themselves do not directly relate to more averaging. In contrast, the Signature1000 bandwidth is fixed and unrelated to the cell size such that larger cell sizes directly relate to more spatial averaging (i.e., the subsamples are independent). We note that the Aquadopp instrument returns correlation as a percentage, which differs from $\hat{R}$ by a factor of 100. We also note the resemblance of Eq. (7) to the equation for standard deviation of phase factor estimates presented in Bendat and Piersol [2011, Eq. (9.91) therein]. This variance estimate assumes a sufficient number of independent samples are used ($N_p \geq 10$), because it relies on the central moment expansion in its derivation and simplification (Shcherbina et al. 2018). Instruments used in this study had $N_p = 10$ and 13 (Table 1) such that this estimate of noise variance is expected to apply, but caution is taken in imposing this estimate of noise on the results.

b. *Spectral signal-to-noise estimates to guide instrument configuration*

Pulse-coherent instruments can be configured to minimize phase wrapping along the measurement profile while maintaining a signal-to-noise ratio (SNR) necessary to estimate

Brought to you by NOAA Central Library | Unauthenticated | Downloaded 11/30/21 04:35 PM UTC

the power in the inertial subrange [Eq. (2)]. Here, we define a spectral SNR based on the estimates presented in Eq. (7) and the expected inertial subrange:

$$\mathrm{SNR} = \frac{C_1 \epsilon^{2/3} k_1^{-5/3}}{\mathrm{var}(V)/k_N}, \tag{8}$$

where the instrument noise is assumed to have a uniform spectral response such that $\mathrm{var}(V)/k_N = \sigma_N^2(k)$, and k_N is the Nyquist wavenumber. The inertial subrange is by its nature a red spectrum, with increasing spectral density at smaller wavenumbers (larger eddy scales). In contrast, the noise is assumed to be white (spectrally uniform). This results in an SNR that is a function of wavenumber, with higher SNR at the low wavenumbers and low SNR at high wavenumbers.

A second constraint can be placed on the instrument during setup to minimize the effects of phase wrapping. It is preferable that no velocity wraps are expected along the profile. This will greatly aid in interpretation and processing of the data, described further in section 2d(1), as no attempt is made to correct for low-mode nonturbulent velocities. Here, we pose the problem such that the standard deviation of the expected turbulent velocities σ_v along the beam is small when compared with the wrapping velocity. We arbitrarily use 4 standard deviations, such that if the velocities are assumed to be Gaussian distributed, roughly 99.99% of velocities would not be expected to wrap because of turbulence. Using the inertial subrange to estimate the standard deviation of velocity gives the constraint,

$$4\left(\int_{k_N}^{k_0} C_1 \epsilon^{2/3} k_1^{-5/3}\, dk\right)^{1/2} \le V_r, \tag{9}$$

where the bounds of integration k_N and $k_0 = 2\pi\ell^{-1}$ are determined by the bin size and the profile length. Note that the profile length is itself constrained by the pulse-to-pulse time lag, and thus is directly related to V_r. Here, we assume the profile length and pulse distance are equivalent. Combining Eqs. (8) and (9), we can show how instrument setup relates to the expected range of TKE dissipation rates. Specifically,

$$4\left(\frac{3}{2} C_1 \epsilon^{2/3}\right)^{1/2} (k_0^{-2/3} - k_N^{-2/3})^{1/2} \le V_r \quad \text{and} \tag{10}$$

$$\frac{\pi^2 N_p (C_1 \epsilon^{2/3} k_1^{-5/3}) k_N}{\mathrm{SNR}(\hat{R}^{-2} - 1)} \gg V_r^2. \tag{11}$$

Noting here that the maximum profile length that sets k_0 is limited by the same pulse distance that limits V_r. The first condition essentially sets the upper bounds of ϵ that can reasonably be measured before phase wrapping starts to modify the along-beam velocity variances. The second represents the ability to resolve an inertial subrange above instrument noise.

A significant caveat to Eq. (11) is that the sample correlation $\hat{R}$ is a diagnostic parameter, and cannot be fully predicted prior to instrument deployment. The returned sample correlations depend on a number of factors specific to the deployment, instrument setup, and local environmental factors, such as the number of scatterers in the water, platform motion and cross-beam flow (Zedel et al. 1996), and the turbulence itself (Shcherbina et al. 2018). For example, one may be tempted to increase the pulse lag and instrument range in an attempt to measure smaller turbulence levels. However, these choices may result in decreased sample correlations (and therefore increased noise) effectively giving poorer resolution. Still, we find Eq. (11) useful to consider during deployment planning, even if intuition with regard to the expected $\hat{R}$ remains an art. We further hope that the configurations and noise levels reported in this study can serve as a guidepost for future, similar deployments.

For this study, the instrument configuration parameters shown in Table 1 resulted in a sufficient number of moderate and larger sample correlations $\hat{R} > 0.6$, which we applied to Eqs. (8) and (9) to estimate typical measurement ranges of $1 \times 10^{-8} < \epsilon < 1 \times 10^{-5}\ \mathrm{m^2\,s^{-3}}$ for the 2-MHz instrument. At high correlation returns, this noise floor may be significantly lower, and measurements of ϵ may be possible 1–2 orders of magnitude lower. The range of wavenumbers and energy levels expected to be resolved by this method are shown with theoretical spectra in Fig. 3. The lower bounds for each box show the white noise estimated from Eq. (7) using correlations of 0.6 and 0.95, respectively. The horizontal extent of the box shows the range of wavenumbers resolved due to the instrument bin size and profile length, which is dependent on the instrument setup and frequency. The upper bound is limited by the unwrapping constraint [Eq. (9)], and spectral energies above this limit would be expected to cause wrapping and are not trusted. Theoretical spectra are shown at three dissipation rates to highlight the resolved portion of the energy spectrum.

c. *ADCP mounting and mechanical deployment*

In the first deployment (Stratus 9 mooring), pairs of ADCPs were mounted to a 1-in.-diameter titanium alloy rod, with pad eye–like attachment points welded to the rod on top and on bottom to allow shackles to tie into the mooring. A fin and swivel system allowed the ADCPs to pivot into the current. On recovery, the 1-in. (2.54 cm) titanium alloy rod fractured where it was welded to the pad eye at the bottom of the 8.4-m ADCP pair, and the mooring line and all instruments deeper than 8.4 m fell to the sea floor. As a result, the deeper ADCP pairs imploded, and their data were lost.

In the subsequent two mooring deployments, ADCP's were mounted to the mooring using Delrin clamps attached to a vertical, weldless titanium alloy flat stock (Fig. 4). The titanium bar is therefore free of welds that created a weak point in the mooring system and led to the catastrophic failure of Stratus 9. The updated mount can attach to the main mooring line directly via shackles at the bar end points. Two Delrin cups screw onto the titanium bar as an attachment point for the Delrin ADCP clamps. Two Delrin figure-8 shaped clamps hold the ADCP's cylindrical body and the Delrin cups attached to the titanium bar. The Delrin cup/Delrin clamp connection is slippery, allowing the clamps to rotate in response to local flow conditions. An orientation fin attaches to the two Delrin

Brought to you by NOAA Central Library | Unauthenticated | Downloaded 11/30/21 04:35 PM UTC

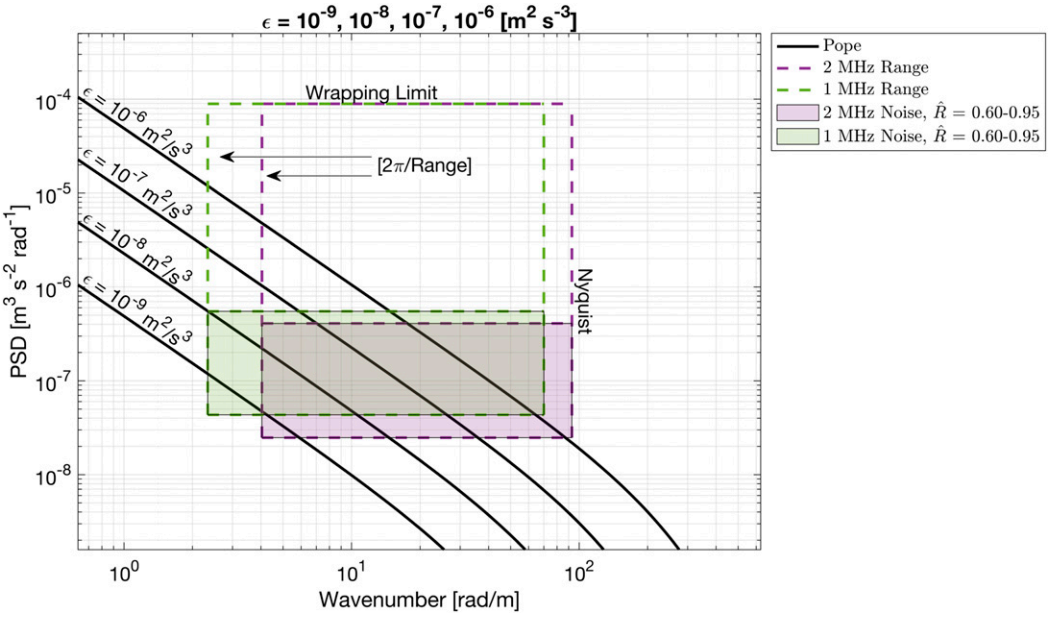

FIG. 3. Example one-sided turbulence spectra for dissipation rates $\epsilon = 10^{-9}$, 10^{-8}, 10^{-7}, and $10^{-6}\,\mathrm{m^2\,s^{-3}}$ for the Pope model spectrum (black). The overlaid dashed boxes show the range of wavenumbers sampled, the maximum spectral estimates due to phase wrapping [Eq. (9)] and the range of white-noise levels predicted by Eq. (7) bounded by the minimum mean along-beam correlations allowed in quality control [see section 2d(2)], and the (roughly) highest returned correlation level ($\hat{R} = 0.6$ and $\hat{R} = 0.95$; shaded boxes). We note that these noise levels are not guaranteed and that it is possible that a mix of different instrument configurations and environmental variables could result in uniformly lower correlations (and thus noise levels). The values here are representative of observed noise levels across multiple mooring deployments used in this study. The color of the dashed boxes differentiates the 1-MHz (green) and 2-MHz (purple) instruments. Based on this parameter space, we expect to resolve the inertial subrange for $\epsilon \sim 10^{-8}$–$10^{-5.5}\,\mathrm{m^2\,s^{-3}}$, with measurement of dissipation rate $\epsilon \sim 10^{-9}$–$10^{-8}\,\mathrm{m^2\,s^{-3}}$ possible with high correlation returns.

clamps opposite the ADCP cylinder, keeping the ADCP body oriented toward the local flow direction. The ADCP is roughly 30 cm from the titanium bar centerline.

d. Data processing

Data processing consists of four primary steps: phase unwrapping, quality control, spectral analysis, and fitting. There are a number of user specific choices during each of these steps, which create a large user parameter space. These choices can significantly modify the resulting estimates of TKE dissipation rate; however, the decision space is too large to explore fully. Instead, we will highlight the effect of many of these choices and discuss how they might compound. Last, we put forward our best advice for processing moving forward.

1) PHASE UNWRAPPING

The pulse-coherent instruments were programmed such that phase wrapping due to turbulence is not expected across the spatial extent of the measurement [via Eq. (9)]. Mean flow, wave orbital motions, and platform motions can easily create flow across the instrument's sampling volume to induce phase wraps from the mean. We seek to estimate along-beam variance, and do not attempt to estimate the mean flow because the mean flow along the beam has no effect on our estimate of the wavenumber spectrum and the dissipation rate. We note that Shcherbina et al. (2018) assessed the value of multiple existing unwrapping methods toward the pulse-coherent acoustic velocimetry problem specifically with respect to the Nortek Signature instrument, and the multicorrelation pulse-coherent processing method. Here, we describe a different method developed parallel to those outlined in Shcherbina et al. (2018). Here, phase wrapping is caused primarily by mean velocities that are much greater than along-beam velocity gradients. The methods in Shcherbina et al. (2018) should arrive at similar solutions to the method outlined here below but were also developed for phase unwrapping under larger velocity gradients.

The approach to unwrapping is to find the minimum variance solution along the beam that is consistent with $V_{\mathrm{unwrap}}(x) = \tilde{V}(x) \pm n(x)V_a$, where $n(x)$ is an integer. Note here that V_r is the maximum unambiguous velocity amplitude, and the wraps range from $-V_r$ to $+V_r$ and vice versa, such that the velocity ambiguity is $V_a = 2V_r$. We process each realization in time independently, using only the spatial structure of the measurements, and proceed as follows. Each measured profile of length M_p is multiplied by nV_a,

Brought to you by NOAA Central Library | Unauthenticated | Downloaded 11/30/21 04:35 PM UTC

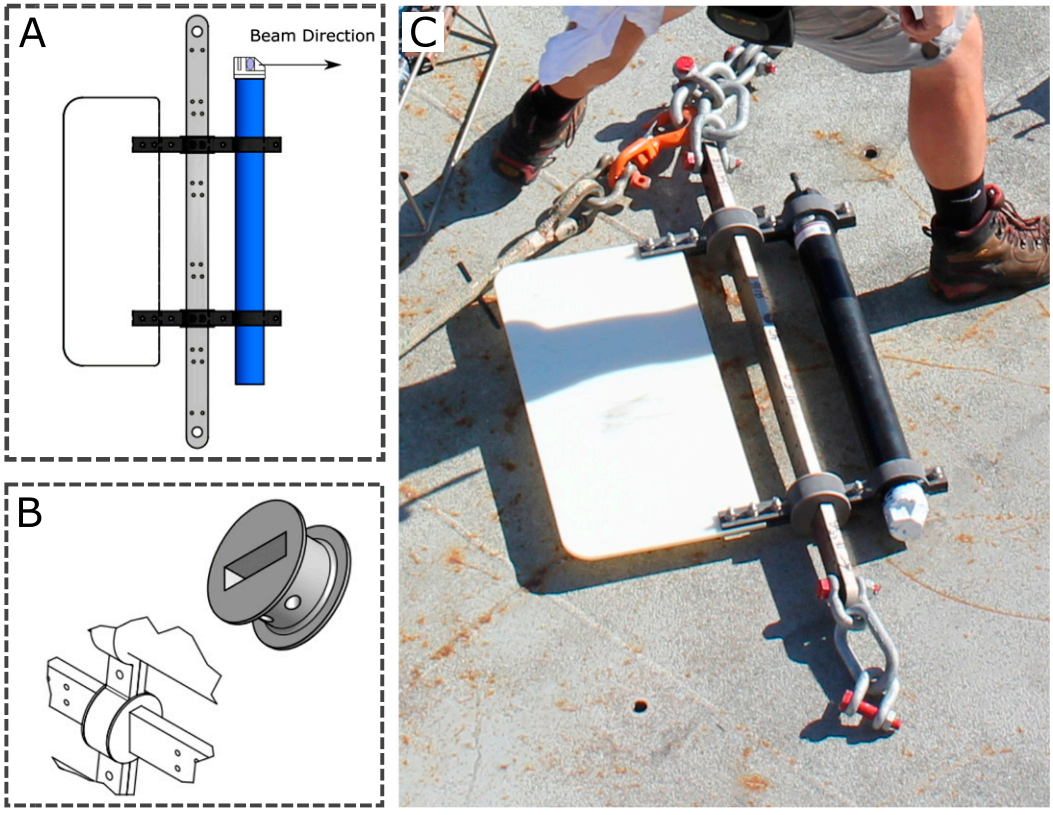

FIG. 4. (a) A side-on view of the Aquadopp mount showing the no-weld titanium bar, Delrin clamps, and orientation fin. (b) The Delrin swivel that attaches the ADCP clamp to the titanium bar. (c) The configured mount on deck before deployment as part of the SPURS-2 mooring. The Aquadopp is equipped with the current-meter transducer head, with the active beam oriented in the horizontal plane pointing upflow from the directional fin.

where $n = [1, 2, 3, 4, 5]$. A histogram is generated for the length $5 \times M_p$ values. If the shear over the ADCP range is less than V_r, the histogram is expected to show groupings of counts consistent with bands of unwrapped solutions, with means offset by V_r. We identify one such grouping through separation of peaks in the histogram using null, or zero-count bins between each grouping. Since the mean velocity will be removed in subsequent spectral analysis, any three of the five expected groupings will provide the solution of interest. An example demonstrating this procedure is shown in Fig. 5. If the along-beam velocity gradient is large and no groupings of histogram counts can be identified, the profile is rejected from further analysis.

2) QUALITY CONTROL

Strong head-on flows can create a region of high pressure at the leading edge of the instrument, leading to flow stagnation. This results in a velocity profile that decreases toward zero velocity as flow approaches the instrument. In a mean-removed profile, the flow distortion results in large positive velocities at low range, with weak negative velocities at farther ranges. This trend is visible in the example unwrapped burst shown in Fig. 5 as a band of positive velocities (colored yellow) in the low range cells. This flow distortion would manifest as low-wavenumber energy in wavenumber spectra that would artificially increase dissipation rate estimates if not dealt with appropriately.

The flow distortion shape is qualitatively consistent with a theoretical model for potential flow around a cylinder, which yields a radial velocity along the flow centerline of the form

$$\frac{V}{V_\infty} = \left(1 - \frac{R^2}{r^2}\right), \tag{12}$$

where V_∞ is the free stream velocity, R is the cylinder radius, and r is the distance from the center of the cylinder. Figure 6 shows a subset of measured velocities in comparison with the mean-removed potential flow model to demonstrate this effect. Here, the cylinder radius is estimated as the distance from the mooring line to the ADCP, roughly 30 cm. Although instrument mount is clearly non-cylindrical (Fig. 4), we note that perturbation solutions for more complex geometries typically have Eq. (12) as the first-order solution, and therefore, it remains a somewhat reasonable approximation.

Brought to you by NOAA Central Library | Unauthenticated | Downloaded 11/30/21 04:35 PM UTC

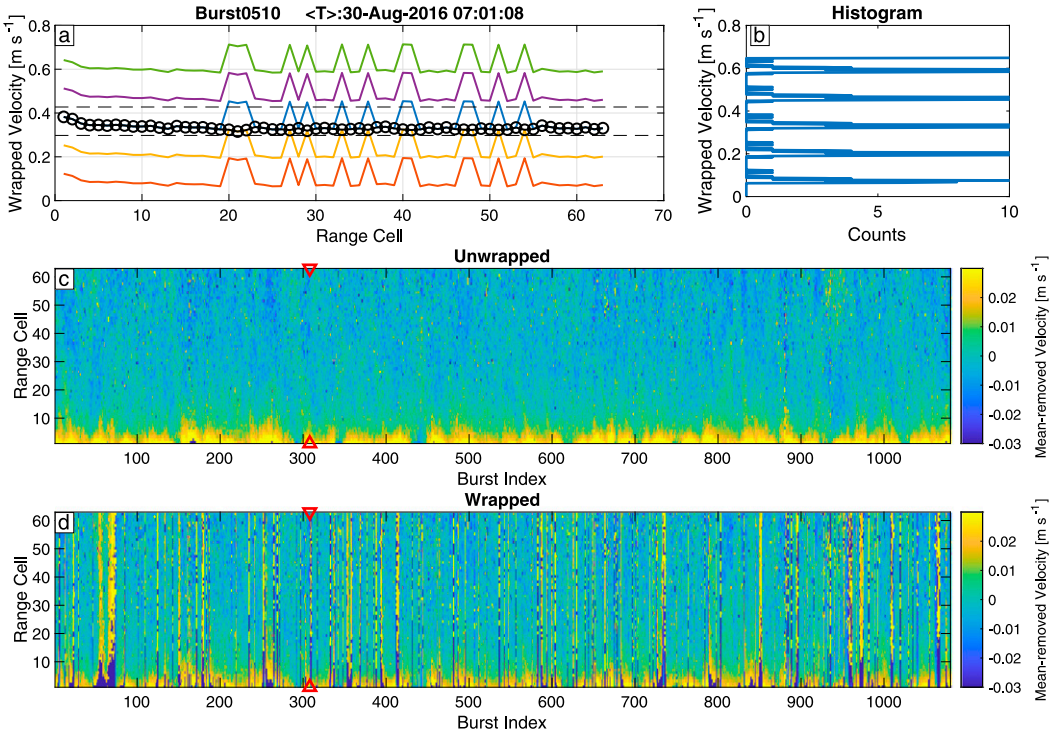

FIG. 5. An example of the unwrapping procedure for an arbitrary burst (SPURS-2; 41.5-m depth). (a) An example of a wrapped profile that has been multiplied by $2nV_r$. The unwrapped profile is shown with the black circles. (b) The histogram used to find the groupings of unwrapped data. (c) The mean-removed unwrapped velocities for the entire burst, consisting of 1080 profiles. (d) The mean-removed wrapped data, shown for comparison. Red triangles mark the specific profile shown in (a) and (b).

To circumvent the introduction of low-wavenumber energy by flow distortion, we choose to remove a subset of the near-sensor data, only allowing distances for which the distorted flow is 90% of the free stream velocity, $v/v_\infty > 0.9$, which is roughly equivalent to 95 cm from the mooring centerline, or the first 18 velocity bins for the 2 MHz instrument. This is an effective extension of the instrument blanking distance to avoid including the spatial signal of flow distortion around the mooring line and instrument mount. The remaining data are linearly detrended, which accounts for the low-slope tail of the flow distortion. The linear trend removal also reduces the energy in the lowest wavenumber of the spectrum, which is not used in subsequent fitting (more on this later).

The Aquadopps were mounted such that they were free to rotate into the flow direction, which is needed to ensure the instrument is looking away from the trailing wake. A more thorough discussion of self-wake contamination by wave orbital motions is presented in the appendix, and here we discuss the effects of platform rotation due to the orbital motions.

The rotational motions are primarily orthogonal to the beam direction, so the velocity estimates themselves are not expected to be biased directly. However, rotational motions can still degrade the velocity measurement in a number of ways. Since the instrument is set up to average a number of ping pairs together, fast instrument rotations blur the direction of the returned averaged values. As a quality control metric, we remove measurements with fast heading rate of changes to limit the directional blurring. We arbitrarily set a max $d\theta/dt = 4\,\mathrm{rad\,s^{-1}}$. We note dissipation rates were not significantly modified by changing this cutoff, but the somewhat loose metric set here resulted in reduced variance of the dissipation rate estimates, likely due to allowance of more profiles in averaging. In part, the effects of rotation are lumped in with data removed due to low correlations. Cross-beam motion (transverse relative velocity) can also degrade the signal, as scatterers in the first acoustic ping are moved out of the sample volume during the subsequent ping. This is directly reflected through lower ping-pair correlations, for example (Zedel et al. 1996, Fig. 8 therein) saw correlations lower to $C = 0.6$ at cross-beam flows of $1\,\mathrm{m\,s^{-1}}$ (although the actual decorrelation likely depends on pulse lag and range).

Profiles and points with low correlations are removed from analysis, following previous studies (Rusello 2009; Thomson 2012). Two distinct correlation criteria were used in this study, the mean along-profile correlations and the correlations associated with measurements at each velocity bin. Profiles with mean along-beam correlations lower than 0.6 are removed from analysis. Of the remaining profiles, individual data points are removed if their correlation is

Brought to you by NOAA Central Library | Unauthenticated | Downloaded 11/30/21 04:35 PM UTC

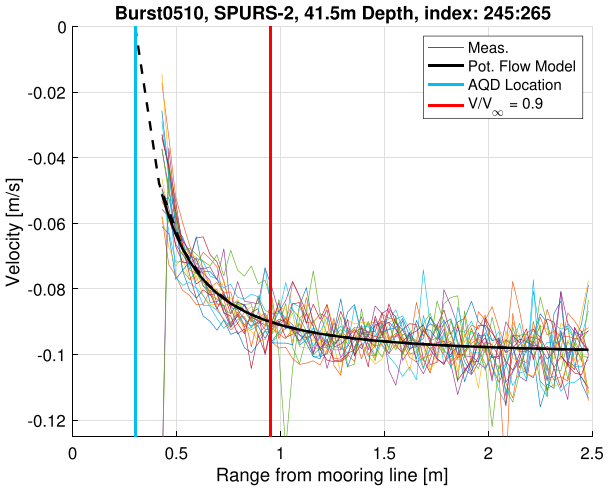

FIG. 6. Example velocity profiles shown in distance from mooring line (thin colors). The potential flow solution for flow around a cylinder with radius of 0.3 m and $V_\infty = 0.1$ is shown in black. The vertical blue line shows the location of the Aquadopp head, 30 cm from the mooring line (equivalent to the estimated cylinder radius), and a vertical red line shows the range where the potential flow is 90% of the free stream velocity, nearly 1 m from the mooring line, and 63 cm from the Aquadopp head. The measured velocity profiles have ambiguous absolute velocity values but are shown here offset by the assumed V_∞ value.

lower than 0.4, and they are replaced via linear interpolation. Profiles with more than two adjacent removed values are not considered for further analysis, as interpolating across multiple removed points can alias variance into the lower wavenumber bands.

Previous studies have also removed data associated with low backscatter, as a low concentration of scatterers can make acoustic velocimetry difficult and be a source of error. Here, we did not observe periods when backscatter was low enough to cause velocimetry to fail, and we will focus on correlation for the main quality control metric. However, attempts to extend the methods presented in this paper to low scattering environments (such as polar regions) may need to include backscatter in data quality assessments.

3) SPECTRAL ANALYSIS

Quality controlled data are used to estimate the wavenumber spectrum of velocities as follows. Following standard spectral analysis techniques, the linear trend of each profile is removed, and each profile is tapered with a Hamming window. A power spectrum is estimated for each profile in the burst, multiplied by a compensation factor to correct for the reduction of variance by the taper (1.59 for a Hamming window), and then averaged to yield a wavenumber spectral estimator. This process is similar to using Welch's method on a time series, with each spatial profile of velocity analogous to a segment from Welch's method. The resulting spectral estimators should then have roughly $2N$ degrees of freedom, where N is the number of profiles that passed quality control.

4) SPECTRAL SLOPE ESTIMATION (REGRESSION)

Computed power spectra are then used to estimate TKE dissipation rate and instrument noise using least squares regression to a model spectrum. Rather than ignoring the presence of noise or imposing a model of the instrument noise in estimating the velocity wavenumber spectrum, we instead choose to estimate both the inertial subrange spectral level and the instrument noise. In this case where we seek estimates of both the signal and the noise, it can be useful to have SNR < 1 at the high wavenumbers such that the noise floor can be estimated from the measurements without need for imposing the Shcherbina et al. (2018) noise model, which will itself have associated error. In this sense, we are effectively viewing both the signal (the inertial subrange spectrum) and the instrument noise as signals to be estimated, because of their different spectral slopes and the fact that we will be fitting to the spectrum over a range of wavenumbers.

The full measured spectrum is expected to have the form

$$\tilde{P}_{11}(k_1) = \mathrm{sinc}\left(\frac{k_1 L_T}{2\pi}\right)^2 \mathrm{sinc}\left(\frac{k_1 L_R}{2\pi}\right)^2 (C_1 \epsilon^{2/3} k_1^{-5/3} + N), \quad (13)$$

from combining a theoretical inertial subrange [Eq. (2)], instrument response [Eq. (6)], and Doppler noise N. A least squares solution is found using MATLAB's "mldivide" function, which solves the matrix equation $\mathbf{Ax} = \mathbf{b}$, with the first column of $\mathbf{A}$ defined as $GC_1 k_1^{-5/3}$, the second column of $\mathbf{A}$ defined as G, where G is the instrument transfer function, and $\mathbf{b} = \tilde{P}_{11}(k_1)$. The two returned elements of $\mathbf{x}$ are then the least squares estimates for $\epsilon^{2/3}$ and N. A subset of the measured wavenumbers are used for the fitting. The lowest wavenumber is removed because its variance is affected by the linear detrend operation applied during spectral processing. Similarly, the four largest wavenumbers are excluded because of the overly large compensation from the transfer function that can cause the variance at those wavenumbers to be artificially large (Fig. 2). Inflated variance at high wavenumbers would cause increased estimates of noise N that would then decrease the value of the estimated TKE dissipation rates.

e. *Example spectral fit*

An example power spectral estimate along with the best fit spectrum are shown in Fig. 7. The spectrum is well fit by the model over most wavenumbers. The recurve due to the spatial sampling filter can be seen around $k_1/(2\pi) \sim 5$ cpm as the measured spectrum decreases at the highest wavenumbers, rather than approaching a flat-sloped white-noise offset. When corrected for transfer function (as was done in Fig. 2), the rolloff to white noise is clearer.

3. Results

a. *Comparison to microstructure data*

Here, we compare the estimated TKE dissipation rates with estimates made from a nearby Slocum glider that

Brought to you by NOAA Central Library | Unauthenticated | Downloaded 11/30/21 04:35 PM UTC

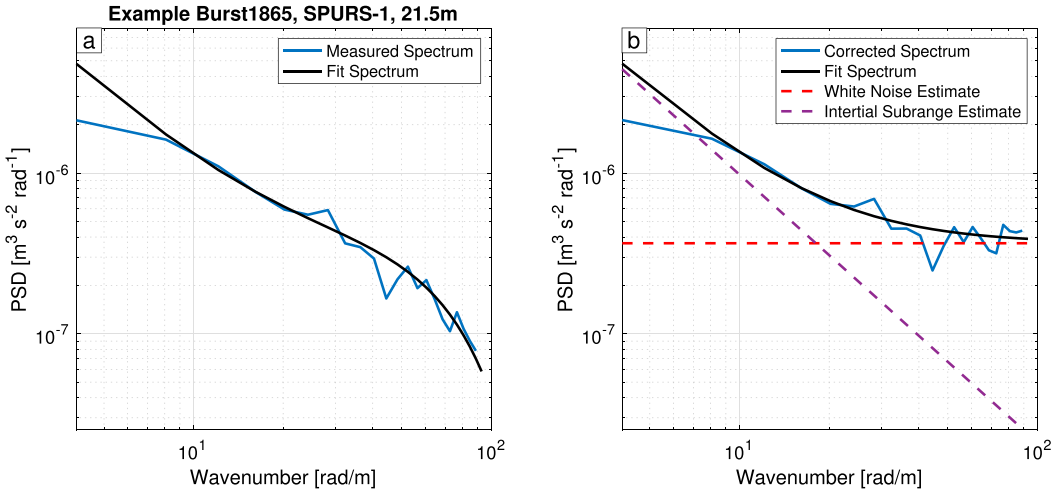

FIG. 7. An example of a spectral fit. (a) The fit includes the sampling filter [e.g., Fig. 2 and Eq. (6)], resulting in the high-wavenumber rolloff despite the existence of white noise. (b) The measured spectrum and fit are corrected for the effect of the sampling filter and are shown with the components of the best fit model, where the estimated white-noise level is shown with the dashed red line and the estimated inertial subrange level is shown with the dashed purple line. The sum of the dashed lines is equal to the solid black best fit determined through regression.

carried a Rockland Scientific Microrider (St. Laurent and Merrifield 2017; Bogdanoff 2017). Glider measurements were taken over the course of 12 days in September–October 2012 within 3–5 km of the mooring location and during a second period for 12 days in March–April 2013. More details on the glider measurements can be found in St. Laurent and Merrifield (2017) and Bogdanoff (2017). Figure 8 shows a comparison of TKE dissipation estimates

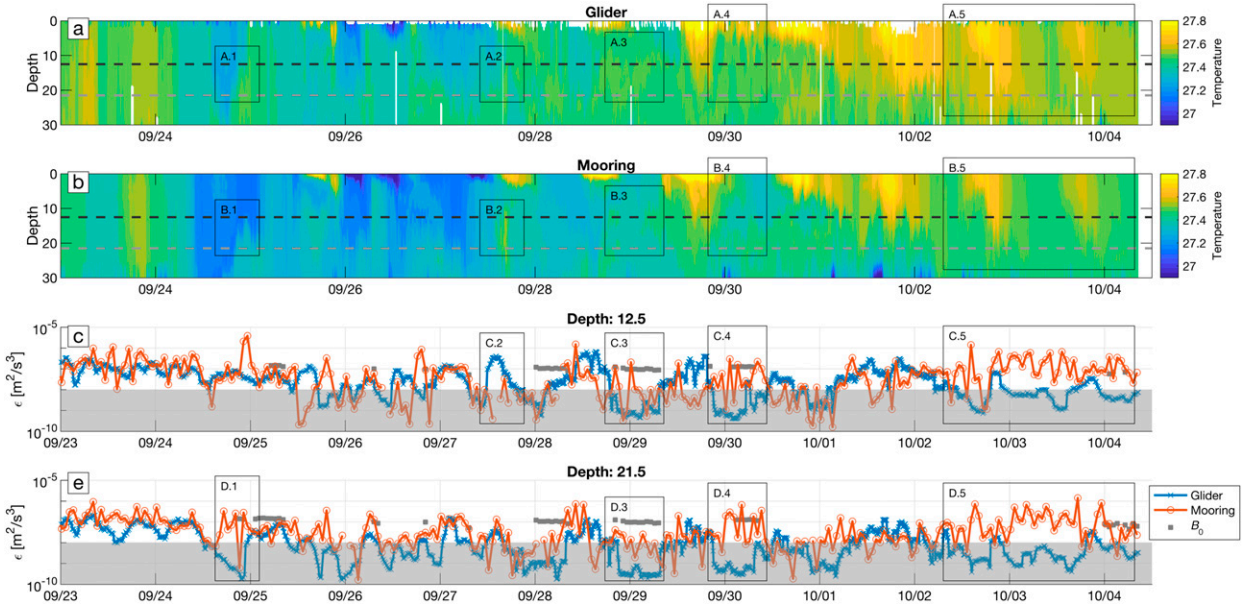

FIG. 8. Depth–time plots of temperature from (a) the glider and (b) the mooring are shown with the TKE dissipation rates at (c) 12.5 and (e) 21.5 m. The largest disagreements between microstructure-derived (glider) and ADCP-derived (mooring) dissipation rates (boxes D.1, C.2, D.2, C.3, and D.3) coincide with differences in temperature profiles, suggesting spatial variability can explain some of the disagreement in dissipation rate estimates. The glider tended to see more temperature stratification (box A.3 compared with box B.3) and lower subsurface dissipation rates during nighttime convection, whereas the mooring temperature profiles showed less stratification, with dissipation rate estimates that were more similar to the surface buoyancy flux B_0.

Brought to you by NOAA Central Library | Unauthenticated | Downloaded 11/30/21 04:35 PM UTC

from the mooring and the glider at 12.5 and 21.5 m along with contour plots of temperature for the 2012 glider deployments. Measurements from glider and mooring are also available at 41.5- and 61.5-m depths but are not compared here. For the duration of the glider deployments, the mixed layer depth varied between 30 and 50 m. Small changes in mixed layer depth over the 2–5-km separation between the measurements would be expected to have a large effect on local TKE dissipation rates, making the comparison difficult.

The turbulence instruments on the mooring and glider have different time–space sampling properties that need to be taken into account to compare the two. The mooring dissipation rate estimates are derived from an average of spectra computed from $O(20)$ 1-m profiles of velocity (collected over 135 s). The glider dissipation rate estimates are made by breaking each vertical profile of the glider into 8-s bins, which translates to roughly 2.5 m of water. These bins are then processed spectrally to form dissipation rate estimates for each bin. Because dissipation rates are approximately log-normally distributed, linear averaging of more estimates or sampling a larger volume will tend to produce higher dissipation rates. The amount of linear averaging is related to the length of time or equivalent volume of water used to estimate velocity or shear spectra, such that longer-duration estimates are likely to estimate larger TKE dissipation rates (closer to the linear expected value of the lognormal distribution). Therefore, the amount of averaging needs to be commensurate for comparing the estimates from the mooring and the glider. Dissipation rates from the glider are smoothed here using an eight-point moving average in time along each depth bin for the comparison to better reflect the volume of water over which dissipation rates are estimated in the mooring-derived estimates (i.e., 80 s and ~20 m for the glider estimates, as compared with 135 s and ~20 m for the mooring estimates). The moving average used here is intended to make the two dissipation estimates more commensurate; however, we acknowledge that there are further subtleties involved in the comparison of turbulence estimates that are beyond the scope of this paper and are not explored further here.

TKE dissipation rates estimated from the mooring compare favorably to the smoothed microstructure-derived estimates from the glider much of the time, as seen in Fig. 8. However, at times the two estimates disagree up to two orders of magnitude (Fig. 8; labeled boxes). Often these disagreements align with differences in the temperature profiles measured at the two sites and may relate to horizontal variability in the vertical stratification of the upper ocean. For example, when the temperature profile indicates near-surface stratification during nighttime convection at the glider sites, the less-stratified mooring-derived dissipation rates are similar to the surface buoyancy flux as predicted by Monin–Obukhov (MO) theory (Fig. 8; boxes C.3, C.4, and D.4). The horizontal variability of stratification and the related differences in TKE dissipation rates are discussed further in section 4a.

A direct comparison of the TKE dissipation rates is shown in Fig. 9, excluding times boxed in Fig. 8. General agreement for glider data above $\epsilon = 10^{-8}\,\mathrm{m^2\,s^{-3}}$ is good. Mooring-derived estimates are biased positively (high) below $\epsilon = 10^{-8}\,\mathrm{m^2\,s^{-3}}$, which is consistent with where ADCP noise variance becomes a large fraction of the total measured spectral variance for the minimum allowed mean correlation returns ($C = 65$; Fig. 3). With low dissipation rates and high noise floor, the ADCP-derived estimates become sensitive to the estimate of the white noise in the spectral fitting. An alternative explanation to the disagreement at $\epsilon = 10^{-8}\,\mathrm{m^2\,s^{-3}}$ is discussed further in section 4b.

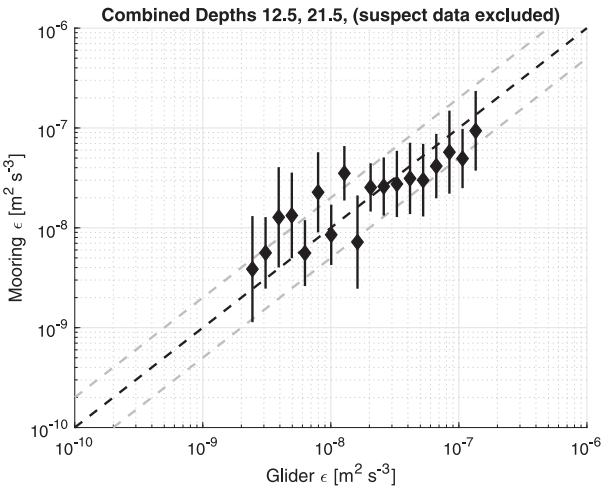

FIG. 9. Direct comparison of time-smoothed microstructure dissipation rates and mooring-derived dissipation rates for both 12.5- and 21.5 m depths. Boxed regions in Fig. 8 have been excluded. Black diamonds represent log-mean bin averages, with associated vertical bars showing the 95% confidence interval of the log mean (1.96 times the standard error). Bin averages with less than 10 values are excluded, and bins were arbitrarily chosen as 40 evenly log-spaced bins on the interval from 10^{-10} to $10^{-6}\,\mathrm{m^2\,s^{-3}}$. The dashed black line shows the 1:1 agreement level. Mooring- and glider-derived dissipation rates agree well above ϵ of $\sim 10^{-8}\,\mathrm{m^2\,s^{-3}}$, below which the mooring-derived estimates appear to be biased. Confidence in the mean is roughly a factor of 2 (gray dashed lines), similar to previous studies (Moum et al. 1995).

A time series of dissipation rates from the 2013 glider deployment is shown in Fig. 10. As in Fig. 8, the glider data have been smoothed to better represent averaging intervals for the estimates. Here, the glider was set to dive deeper than in the 2012 deployment, and therefore, comparisons are shown to 122 m. All depths show some agreement between the two estimates, with the best agreement at the shallow depth instruments. Agreement is particularly strong during the last three glider deployment days (3–5 April), with both methods showing similar trends over roughly four orders of magnitude of TKE dissipation rate. Similar to Fig. 9, a direct comparison for the second deployment (Fig. 11) shows good agreement on average above $\epsilon = 10^{-8}\,\mathrm{m^2\,s^{-3}}$, with the mooring biased positively (high) relative to the glider estimates of ϵ below $\epsilon = 10^{-8}\,\mathrm{m^2\,s^{-3}}$.

Brought to you by NOAA Central Library | Unauthenticated | Downloaded 11/30/21 04:35 PM UTC

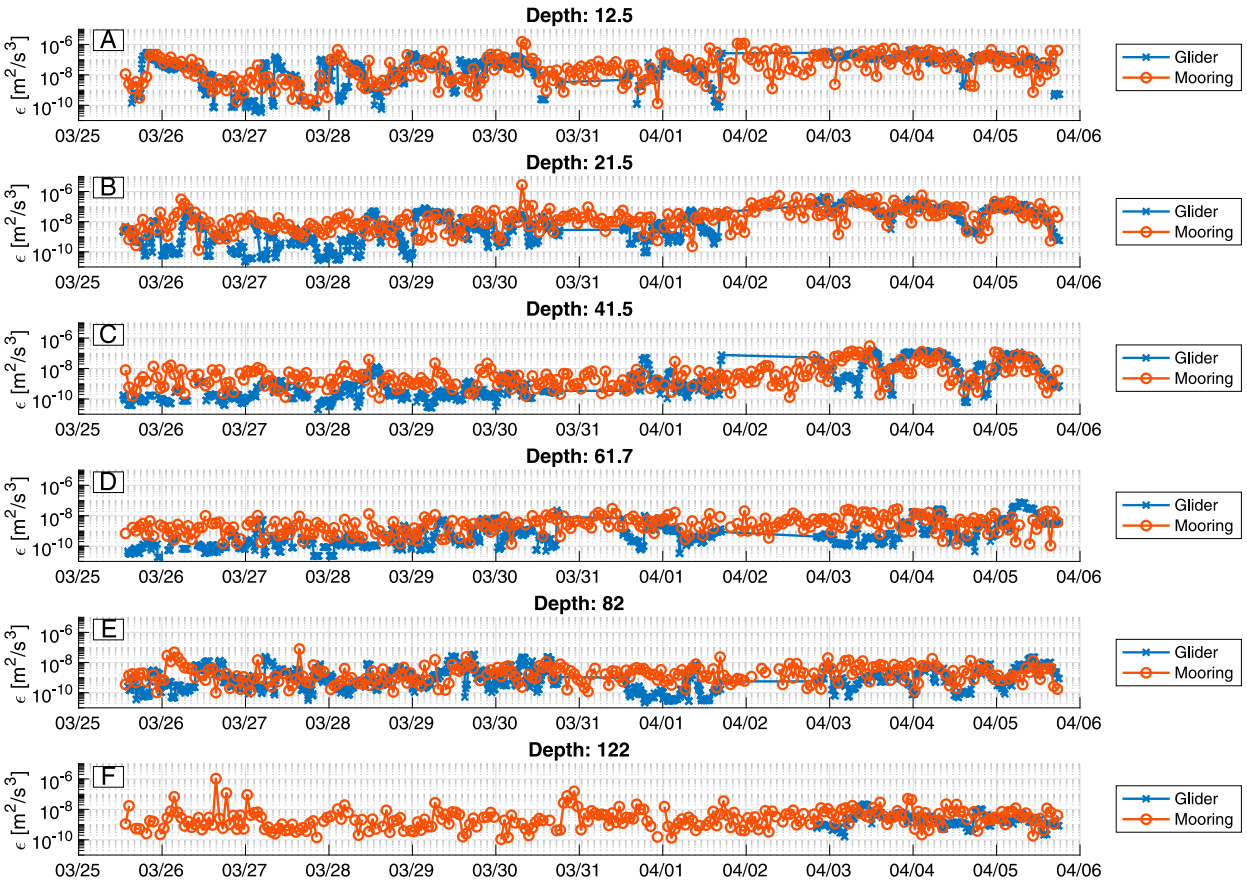

FIG. 10. Comparison of time-smoothed glider-derived microstructure dissipation rates and mooring-derived dissipation rates for all depths during the second glider deployment in March and April 2013. Measurements at depths of 12.5, 21.5, 41.5, 82, and 122 m were made by 2-MHz instruments, with measurements at 61.7 m made by a 1-MHz instrument. Agreement between the glider and mooring measurements is best during 3–6 Apr.

b. *Comparison with surface buoyancy flux*

The comparisons of the new method for estimating TKE dissipation rates with microstructure shown in Figs. 8 and 9 are limited in scope, only covering 12 days of the multiple years of data available using the new method. As a further check on the validity of the new estimates, we compare mooring-derived dissipation rates with measurements of surface fluxes from the same mooring. Under MO theory, the upper-ocean dissipation rate should equal the surface buoyancy flux B_0 under strong convection defined with the MO similarity parameter z/L (Wyngaard and Coté 1971), with $L = u_*^3/(c_{vk}B_0)$, where u_* is the friction velocity and c_{vk} is von Kármán's constant. Here, we compare surface buoyancy fluxes and TKE dissipation rates from the measurement nearest the surface (12.5 m for SPURS-1; 7 m for SPURS-2). We limit the comparison to periods for which we expected $\epsilon = B_0$, which we set as $z/L < -5$, and $z/\mathrm{MLD} < 0.75$. Comparisons are shown in Fig. 12.

TKE dissipation rates agree with surface buoyancy fluxes in the mean for near-surface depths for both SPURS-1 and SPURS-2 deployments. In both cases, choosing $z/L < -5$ primarily limits $B_0 > 10^{-8}\,\mathrm{m^2\,s^{-3}}$, coinciding with the range of values over which mooring-derived dissipation estimates were unbiased when compared with shear-microstructure estimates (Figs. 9 and 11).

c. *Long duration time series*

Contours of the TKE dissipation rate for the duration of the SPURS-1 mooring are shown in Fig. 13. The TKE dissipation rates are generally larger near the surface, and larger above a mixed layer depth estimated from temperature (defined as the depth at which temperature is 0.05°C different from the surface value). The $\epsilon < 10^{-8}\,\mathrm{m^2\,s^{-3}}$ contour, near the range of values often used to define a turbucline (Clayson et al. 2019) or a mixing layer depth (Sutherland et al. 2014) is consistently near the mixed layer depth, particularly when the mixed layer is deepening. This is qualitatively consistent with previous studies that show the mixed layer depth and the depth of active mixing are often similar, but not always the same (Brainerd and Gregg 1995). This can be seen on seasonal scales (Fig. 13a), as the mixed layer depth deepens from October to December 2012 and then shallows again over the spring/summer of 2013.

Brought to you by NOAA Central Library | Unauthenticated | Downloaded 11/30/21 04:35 PM UTC

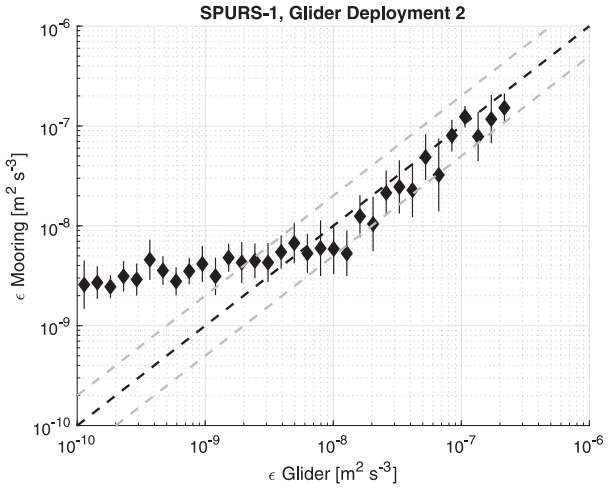

FIG. 11. Direct comparison of time-smoothed microstructure dissipation rates and mooring-derived dissipation rates for all depths (12.5, 21.5, 41.5, 61.7, 82, and 122 m) during the second glider deployment in March and April 2013. The vertical bars show the 95% confidence interval of the log mean (1.96 times the standard error). Bin averages with less than 10 values are excluded, and bins were arbitrarily chosen as 40 evenly log-spaced bins on the interval from 10^{-10} to 10^{-6}. The dashed black line shows the 1:1 agreement level. As in Fig. 9, agreement between the two dissipation rate estimates is good above $\epsilon = 10^{-8}\,\mathrm{m^2\,s^{-3}}$.

The qualitative agreement between dissipation contours and mixed layer depths can also be seen over diurnal cycles (Fig. 13b), as exemplified by classic pattern of nighttime convection and daytime stratification in May 2013. TKE dissipation rates below the mixed layer are generally less than $10^{-8}\,\mathrm{m^2\,s^{-3}}$, which is close to the noise floor of our estimates (as indicated in Fig. 9).

4. Discussion

The agreement between glider-derived and mooring-derived TKE dissipation rates in this study is similar to the results from Moum et al. (1995), which compared estimates of TKE dissipation rates from independent shear probes located between 1 and 11 km apart, with little upper-ocean differences between the two sites. In their study, Moum et al. (1995) found the two sets of TKE dissipation rate measurements showed significant variability at short time scales, with individual data pairs differing by 1–2 orders of magnitude. However, they also found that hourly averages showed significant correlation, and histograms of the two datasets at some, but not all depths, were statistically likely to be derived from the same distribution, determined through a two-sample χ^2 test. Moum et al. (1995) attributed the variability between estimates at the two sites to be related to natural variability of turbulence and suggested that the systematic bias of the dissipation rate estimates was roughly a factor of 2.

The comparison between the mooring-derived TKE dissipation rates and glider-derived TKE dissipation rates in this study have many similarities to Moum et al. (1995). TKE dissipation rates differ at times by several factors of 10 (Fig. 8; boxes), but there is agreement in the mean above $\epsilon \approx 10^{-8}\,\mathrm{m^2\,s^{-3}}$ with 95% confidence bars suggesting mean bias roughly a factor of 2. Following Moum et al. (1995), we conducted a two-sample χ^2 test finding that at most depths (with the exception of the 21-m comparison) the mooring and glider estimates of TKE dissipation rates are unlikely to be derived from different distributions at a 95% significance level (here, the test was restricted to values above $\epsilon \approx 10^{-8}\,\mathrm{m^2\,s^{-3}}$). Next, we will discuss potential explanations for the occasional discrepancies between the glider- and mooring-based observations.

a. *Horizontal variability of surface stratification and TKE dissipation rates in SPURS-1*

In contrast to the Moum et al. (1995) study, times of largest disagreement between the two estimates seem to be associated with differences in the vertical structure of temperature between the two sites. These differences cause either the glider estimates to be larger in comparison with the mooring estimates (Fig. 8; box C.2), or vice versa (Fig. 8; boxes C.3, C.4, C.5, D.1, D.3, D.4, and D.5). That the differences are seen in both directions (e.g., mooring estimates could be larger or smaller than glider estimates) provides further support for natural variability. However, we do note that these differences occur more frequently as mooring estimates larger than glider estimates, which could reflect the limitations of the mooring estimates to capture small dissipation rates, or a sampling bias (rather than instrument bias) between the two estimates due to mesoscale flow features over the 2 weeks of sampling.

Regardless, disagreement between the mooring dissipation rates and the glider dissipation rates do seem to occur with differences in glider and mooring temperature profiles (boxes, Fig. 8). These temperature differences are indicative of differences in vertical stratification that modify the local TKE dissipation rates, and their relation to the local surface fluxes. As shown in Fig. 14, satellite-derived SST products [VIIRS NPP; NOAA Office of Satellite and Product Operations (OSPO); NOAA OSPO 2019] confirmed temperature differences on 2-km scales similar to the glider–mooring differences (ΔT of 0.1°–0.2°C), which gives further reason to believe these temperature differences are real, and not simply instrument error.

Boxes B.2, A.3, and A.5 in Fig. 8 all show temperature inversions that are indicative of the existence of barrier layers. Associated with these temperature inversions are dissipation rates that are smaller than the nearby measurement with weaker or nonexistent temperature inversions. That is, mooring dissipation rates in box C.2 are smaller than the glider estimates, and the mooring sees a larger temperature inversion (box B.2) than in the glider data (box A.2). Similarly, glider dissipation rates are smaller than the mooring estimates in boxes C.3, D.3, C.5, D.5, where temperature inversions exist in the glider data (boxes A.3 and A.5) but not the mooring data (boxes B.3 and B.5). During these periods when nighttime convection was strong, the

Brought to you by NOAA Central Library | Unauthenticated | Downloaded 11/30/21 04:35 PM UTC

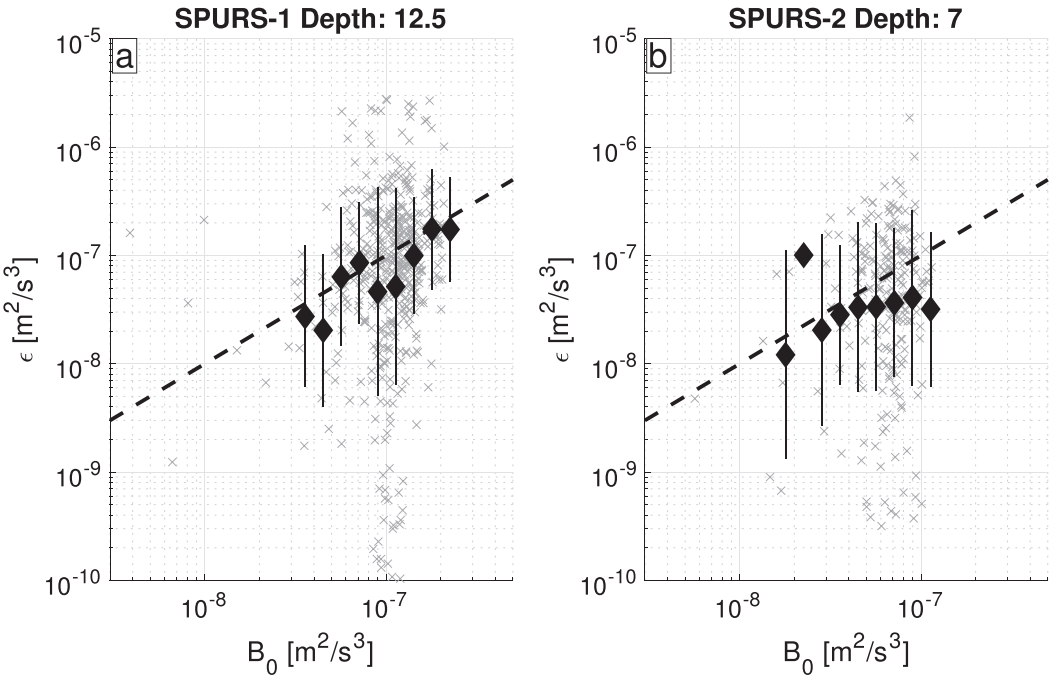

FIG. 12. Upper (a) SPURS-1 and (b) SPURS-2 dissipation rate estimates in comparison with surface buoy estimates of surface buoyancy flux (COARE) during strong convective conditions $z/L < -5$ and above the mixed layer depth $z/\mathrm{MLD} < 0.75$. Data arbitrarily binned with 35 even intervals in log space between 10^{-9} and 10^{-6} are shown as solid black diamonds, with vertical bars showing 1 standard deviation within the bin. Bin averages are only shown if they contain more than 10 data points.

mooring TKE dissipation rates were similar to the surface buoyancy flux as expected from boundary layer theory.

Differences in mooring and glider dissipation rates in boxes C.4, D.4 correspond with the existence of a warm near-surface layer in the glider data (box A.4) not seen in the mooring data (box B.4). Here, the mooring dissipation rates follow the expected boundary layer theory for strong nighttime convection and are similar to the surface buoyancy flux. The existence of the near-surface temperature stratification in the glider data may indicate the importance of horizontal gradients and/or advection.

Differences seen in boxes A.1, B.1, and D.1 seem to be associated with deviations of the size and arrival time and depth of temperature stratification seen in both glider and mooring data. Differences in TKE dissipation rates at the 12.5-m depth are minimal during this period.

b. *Noise floor or anisotropy?*

The mooring-derived TKE dissipation rates agree with the glider-derived TKE dissipation rates down to $\epsilon = 10^{-8}\,\mathrm{m^2\,s^{-3}}$ for both glider deployments, as shown in Figs. 9 and 11. Given the noise levels suggested from Eq. (7) (Shcherbina et al. 2018), as presented graphically in Fig. 3 (shaded boxes), it is likely that this energy level is simply too close to the noise floor of the ADCP. Given the advances of newer signal processing software to improve velocity wrapping range and to increase instrument bandwidth [e.g., Nortek Signature1000 as discussed in Shcherbina et al. (2018)], newer ADCPs likely can measure a larger dynamic range of ϵ.

An alternate hypothesis is that the assumption of an isotropic inertial subrange breaks down where stratification limits low-wavenumber energy, and the imposed turbulence model is no longer valid. In other words, the application of Eq. (2) cannot be made, since the shape function $f_L(\kappa L)$ is no longer close to 1. Under stratified turbulence, the Ozmidov scale $L_{\mathrm{oz}} = \epsilon^{1/2}/N^{3/2}$, where N is the buoyancy frequency, is often used to describe the largest vertical eddy scale. Using stratification and dissipation rates from the glider, Ozmidov scales were in the range $10^{-1} \leq L_{\mathrm{oz}} \leq 10^{2}\,\mathrm{m}$, as compared with the ~1.5-m pathlength used by the mooring-mounted ADCPs. Because of the small range of stratification measured during the glider deployment, the $L_{\mathrm{oz}} \sim 1\,\mathrm{m}$ limit corresponds to $\epsilon \sim 10^{-8}\,\mathrm{m^2\,s^{-3}}$, similar to the estimate of the ADCP noise floor. The glider-derived dissipation rates are made closer to the Kolmogorov scale and would be less sensitive to the Ozmidov scale rolloffs. In contrast, the mooring-derived estimates rely on the slightly longer, more energetic scales that are more quickly affected by limiting buoyancy.

The exact cause of the disagreement between the two dissipation estimates is somewhat ambiguous, as both anisotropy and the ADCP noise levels that start to affect the results occur at glider-measured $\epsilon \sim 10^{-8}\,\mathrm{m^2\,s^{-3}}$. Future work to improve ADCP-derived estimates of turbulence would benefit from both lower spectral noise, and the possibility of including local estimates of stratification in the theoretical spectrum, which

Brought to you by NOAA Central Library | Unauthenticated | Downloaded 11/30/21 04:35 PM UTC

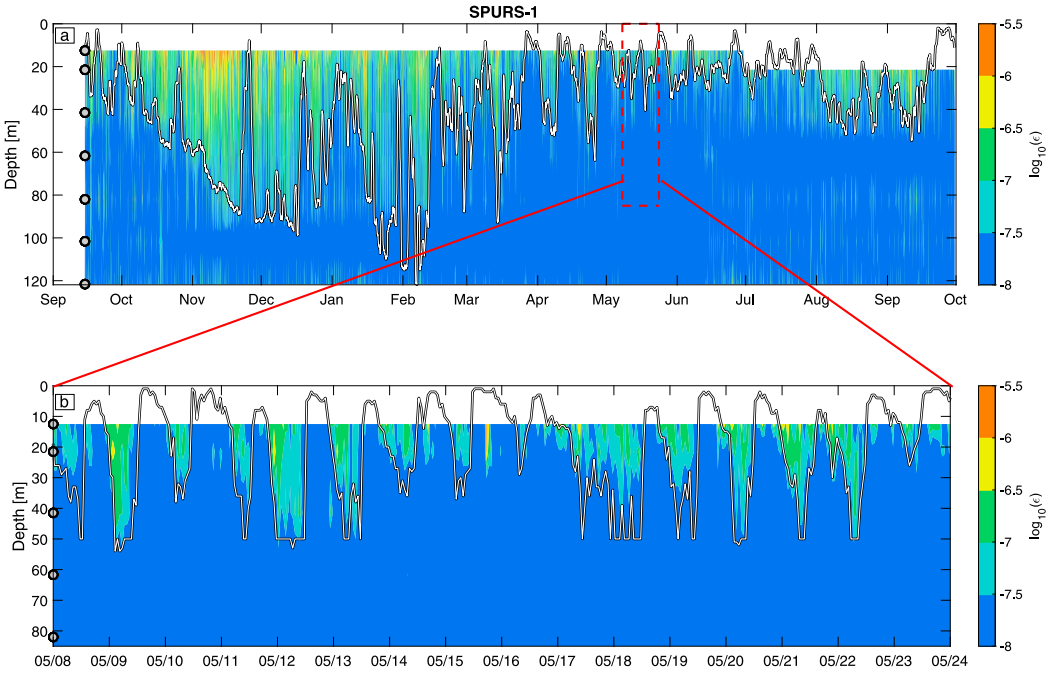

FIG. 13. Contour plots of TKE dissipation rate estimates for SPURS-1, with the depth of the estimates shown with gray circles to the left. Hourly estimates of mixed layer depth are shown above the contours (estimated as the depth at which temperature is 0.05°C different from the surface value), with (a) 24-h moving mean for clarity. The full duration results in (a) generally show that dissipation rates are larger above the temperature-estimated mixed layer depth. (b) Diurnal variability in TKE dissipation rates are seen to be consistent with the variability in the mixed layer depth. Missing values have been interpolated in (a) and (b).

will help to push confidence in the measurement below $\epsilon \sim 10^{-8}\,\mathrm{m^2\,s^{-3}}$.

5. Summary

We present a method for estimating TKE dissipation rates from pulse-coherent ADCPs on deep-ocean moorings. We overview practices for programming the ADCP to ensure a range of measurable TKE dissipation rates and present a mount for minimizing the chance of mooring failure, and self-wake contamination. We also overview data quality control, spectral methods, flow contamination, and an estimate of the instrument's spectral response function needed to apply inertial subrange fits to mooring-measured velocity wavenumber spectra.

We find TKE dissipation rates estimated with the method outlined in this paper compare favorably to measurements made with a microstructure shear probe on a nearby glider for $\epsilon \sim 10^{-8}\,\mathrm{m^2\,s^{-3}}$ and larger. The comparison between nearby TKE dissipation rate estimates in this study are similar to those between two microstructure shear probes in past studies, which have suggested natural variability often causes hourly averages of ϵ to differ by several factors of 10, but with systematic bias less than a factor of 2 (Moum et al. 1995). In this study, periods of disagreement between the glider-derived dissipation rates and the mooring-derived dissipation rates are associated with differences in the vertical temperature profiles at both locations (horizontal scales of 2–5 km). This may indicate the importance of small-scale horizontal processes in setting upper-ocean turbulence.

Upper-ocean TKE dissipation rate estimates and the locally measured surface buoyancy flux agreed in the mean during periods of strong convection when the instruments were above

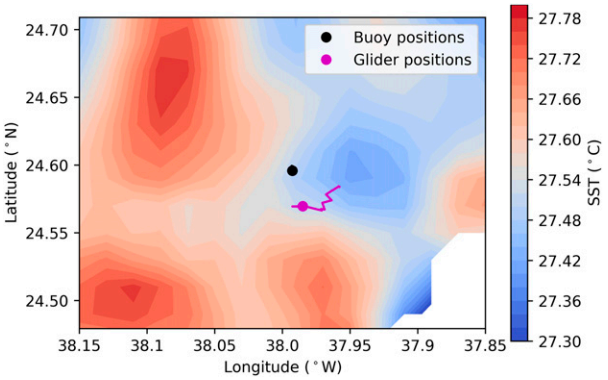

FIG. 14. Satellite-derived SST taken at 0330:02 UTC 30 Sep 2012 is shown with positions of the SPURS-1 central mooring and the glider track during the September–October sampling period (i.e., the data shown in Fig. 8). SST variability on the order of 0.2°C exists over small scales, suggesting that some of the differences in local water properties and turbulent statistics seen between the mooring and glider datasets are physical rather than manifestations of sensor or methodological errors.

Brought to you by NOAA Central Library | Unauthenticated | Downloaded 11/30/21 04:35 PM UTC

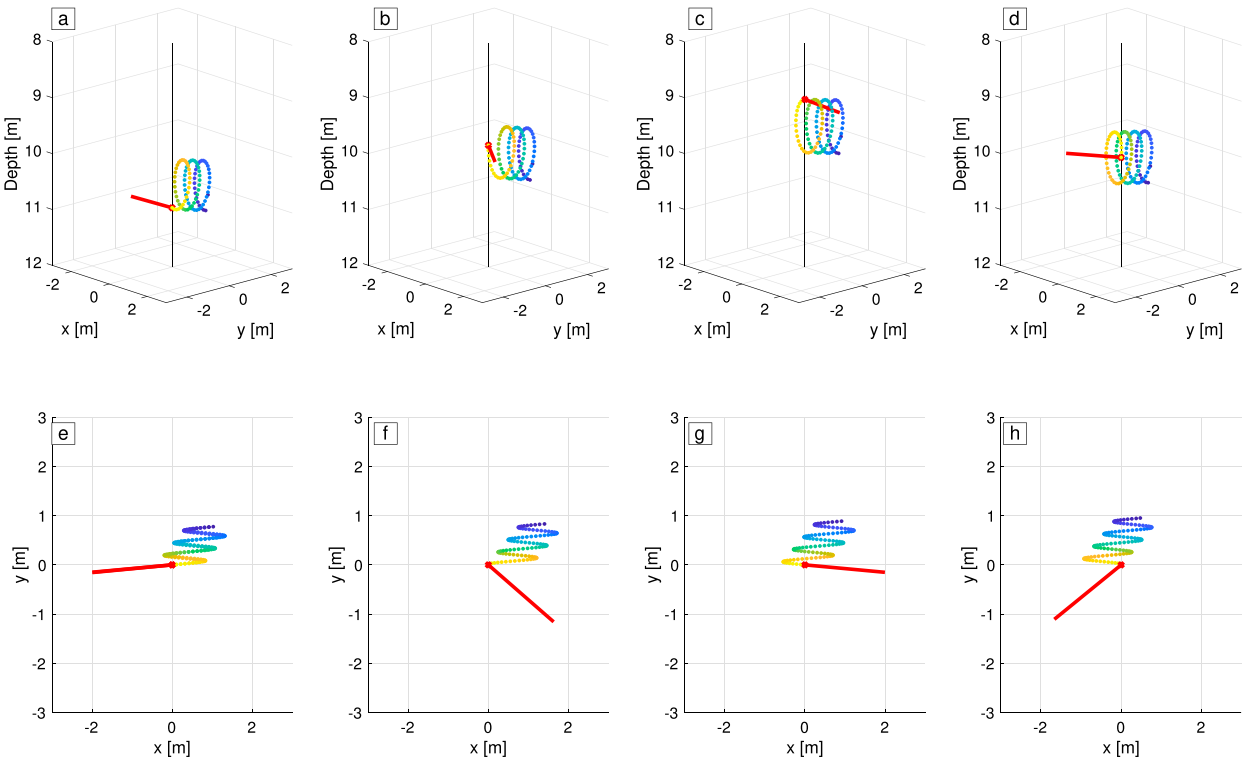

FIG. A1. Four phases of a simulated wake with monochromatic waves and a constant off-wave angled mean velocity. (a)–(d) Snapshots of the 3D view of the wake at four unique phases. (e)–(h) A top-down 2D view during the same phases as in (a)–(d). The red line shows the upflow direction mimicking the expected orientation of the ADCP. The yellow-to-blue circles show a simulated wake, with locations determined through the advection of the previous instrument locations. The simulated wake's color scale indicates timing of wake creating. The vertical line in (a)–(d) shows a reference mooring line. Here, simulated 8-s-period 2-m-in-height monochromatic waves propagate in the positive x direction, with a small mean cross flow ($U_y/U^{\mathrm{orb}} = 0.075$, $U_y = 0.03\ \mathrm{m\ s^{-1}}$) in the positive y direction. At no part of the wave period does the simulated ADCP beam intersect the wake.

mixed layer depths, consistent with boundary layer theories. Vertical gradients in TKE dissipation rates were qualitatively consistent with mixed layer depths, showing large decreases in dissipation rates below the mixed layer depths on both seasonal and diurnal time scales.

Acknowledgments. This work was funded by NASA as part of the Salinity Processes in the Upper Ocean Regional Study (SPURS), supporting field work for SPURS-1 (NASA Grant NNX11AE84G), for SPURS-2 (NASA Grant NNX15AG20G), and for analysis (NASA Grant 80NSSC18K1494). Funding for early iterations of this project associated with the VOCALS project and Stratus 9 mooring was provided by NSF (Awards 0745508 and 0745442). Additional funding was provided by ONR Grant N000141812431 and NSF Award 1756839. The Stratus Ocean Reference Station is funded by the Global Ocean Monitoring and Observing Program of the National Oceanic and Atmospheric Administration (CPO FundRef Number 100007298), through the Cooperative Institute for the North Atlantic Region (CINAR) under Cooperative Agreement NA14OAR4320158. Microstructure measurements made from the glider were supported by NSF (Award 1129646). We also thank Andrey Shcherbina, Jim Edson, and Carol Anne Clayson for helpful discussions on Nortek instruments, spectral analysis, and boundary layer turbulence.

Data availability statement. Data from the SPURS moorings including the processed dissipation rates are available through NASA's PO.DAAC (https://podaac.jpl.nasa.gov/; https://doi.org/10.5067/SPUR1-MOOR1 for SPURS-1, https://doi.org/10.5067/SPUR2-MOOR1 for SPURS-2) and through WHOI's UOP website (http://uop.whoi.edu/projects/SPURS/spurs.html). Code used to process TKE dissipation rates and generate the figures is available on github (https://github.com/zippelsf/MooredTurbulenceMeasurements). Intermediate data products used in making figures are available on Zenodo (https://doi.org/10.5281/zenodo.5032511).

APPENDIX

Wave Orbital Motions and Self-Wake Contamination

Large wave orbital motions have the ability to bring the turbulent wake of the mooring back in front of the sample volume of the ADCP, potentially contaminating and artificially increasing the turbulence estimate from the ambient value. Even for vaned instruments that look into the flow, flow reversal due to large local orbital velocities can cause the instrument to reverse directions and point toward the mean downstream direction. A rough estimate of the impact of wave

Brought to you by NOAA Central Library | Unauthenticated | Downloaded 11/30/21 04:35 PM UTC

orbital motions on advection at the ADCP location is the local ratio of mean velocity to rms wave orbital velocity. Here, we estimate RMS wave orbital velocity from the surface elevation power spectral density, $E(\omega)$, provided by the wave package on the surface mooring. Assuming deep water waves and linear dispersion, the wave orbital variance is

$$U_{\mathrm{rms}}^{\mathrm{orb}} = \left[\int \omega^2 E(\omega)\, \exp(-z\omega^2/g)\, d\omega\right]^{1/2}. \tag{A1}$$

Using this definition, we find the ratio of mean advection to rms wave orbitals, $\overline{U}/U_{\mathrm{rms}}^{\mathrm{orb}}$, to be primarily between 0.1 and 1 for the near-surface locations (less than 20-m depth) and primarily between 1 and 10 for deeper locations. The surface locations, therefore, are most suspect because of having $\overline{U}/U_{\mathrm{rms}}^{\mathrm{orb}} < 1$. However, $\overline{U}/U_{\mathrm{rms}}^{\mathrm{orb}} < 1$ does not mean all observations from these locations must be thrown out. The 3D nature of the wake, and the highly directional wave orbital motions, can make self-wake contamination unlikely, even when $\overline{U}/U_{\mathrm{rms}}^{\mathrm{orb}} < 1$.

To demonstrate the challenge of self-wake contamination with a small cross flow, we pose a simplified model below. Here, we set a small mean flow ($\overline{U}/U_{\mathrm{rms}}^{\mathrm{orb}}) < 0.1$ at 45° to a simulated monochromatic wave to demonstrate how this small cross-flow component results in no self-wake contamination. We assume the mooring does not move horizontally but is fixed to the free surface and moves with the vertical heave of the surface (i.e., the mooring line is inelastic). We use wave and depth parameters similar to what is expected for moderate wave conditions at the near-surface ADCP, with $H = 2$ m, $T = 8$ s, and mean instrument depth of $z = 10$ m. We set the local mean flow to $\overline{U}/U_{\mathrm{rms}}^{\mathrm{orb}} < 0.1$ at depth, resulting in a 0.03 m s^{-1} cross-wave flow component. An example of the wake created from an instrument at 10 m by a monochromatic wave field with small cross flow is shown in Fig. A1.

While this simulation is highly idealized, it indicates that the relative current/wave direction is important in understanding self-wake contamination. The directional spread of waves tends to be larger for short waves (at higher frequency) whose orbital motions decay quickly with depth. Furthermore, mean currents at depth are unlikely to be in perfect alignment with the dominant low-frequency wave direction due to a variety of factors. Future work is needed to better characterize mooring self-wake, and should consider the relative wave current direction, as well as the directional spread of the wave field. Nonetheless, self-wake contamination seems less likely than we had feared because 1) the ADCP is moving up and down with the sea surface, 2) the instrument heading is varying with wave phase, and 3) the mean cross-wave flow is generally nonzero.

REFERENCES

Bendat, J. S., and A. G. Piersol, 2011: *Random Data: Analysis and Measurement Procedures*. Vol. 729, John Wiley and Sons, 640 pp.

Bogdanoff, A. S., 2017: Physics of diurnal warm layers: Turbulence, internal waves, and lateral mixing. Ph.D. thesis, Massachusetts Institute of Technology, 179 pp.

Brainerd, K. E., and M. C. Gregg, 1995: Surface mixed and mixing layer depths. *Deep-Sea Res. I*, **42**, 1521–1543, https://doi.org/10.1016/0967-0637(95)00068-H.

Clayson, C. A., J. B. Edson, A. Paget, R. Graham, and B. Greenwood, 2019: Effects of rainfall on the atmosphere and the ocean during SPURS-2. *Oceanography*, **32** (2), 86–97, https://doi.org/10.5670/oceanog.2019.216.

Comte-Bellot, G., and S. Corrsin, 1971: Simple Eulerian time correlation of full-and narrow-band velocity signals in grid-generated, 'isotropic' turbulence. *J. Fluid Mech.*, **48**, 273–337, https://doi.org/10.1017/S0022112071001599.

Dillon, J., L. Zedel, and A. E. Hay, 2012: On the distribution of velocity measurements from pulse-to-pulse coherent Doppler sonar. *IEEE J. Oceanic Eng.*, **37**, 613–625, https://doi.org/10.1109/JOE.2012.2204839.

Edson, J. B., and Coauthors, 2013: On the exchange of momentum over the open ocean. *J. Phys. Oceanogr.*, **43**, 1589–1610, https://doi.org/10.1175/JPO-D-12-0173.1.

Fairall, C., E. Bradley, J. Hare, A. Grachev, and J. Edson, 2003: Bulk parameterization of air–sea fluxes: Updates and verification for the COARE algorithm. *J. Climate*, **16**, 571–591, https://doi.org/10.1175/1520-0442(2003)016<0571:BPOASF>2.0.CO;2.

Farrar, J. T., and A. J. Plueddemann, 2019: On the factors driving upper-ocean salinity variability. *Oceanography*, **32** (2), 30–39, https://doi.org/10.5670/oceanog.2019.209.

——, and Coauthors, 2015: Salinity and temperature balances at the SPURS central mooring during fall and winter. *Oceanography*, **28** (1), 56–65, https://doi.org/10.5670/oceanog.2015.06.

Fisher, A. W., L. P. Sanford, and M. E. Scully, 2018: Wind-wave effects on estuarine turbulence: A comparison of observations and second-moment closure predictions. *J. Phys. Oceanogr.*, **48**, 905–923, https://doi.org/10.1175/JPO-D-17-0133.1.

Gargett, A. E., 1994: Observing turbulence with a modified acoustic Doppler current profiler. *J. Atmos. Oceanic Technol.*, **11**, 1592–1610, https://doi.org/10.1175/1520-0426(1994)011<1592:OTWAMA>2.0.CO;2.

Gemmrich, J., 2010: Strong turbulence in the wave crest region. *J. Phys. Oceanogr.*, **40**, 583–595, https://doi.org/10.1175/2009JPO4179.1.

Kolmogorov, A. N., 1941: Dissipation of energy in the locally isotropic turbulence. *Dokl. Akad. Nauk SSR*, **30**, 301–305.

Lueck, R. G., D. Huang, D. Newman, and J. Box, 1997: Turbulence measurement with a moored instrument. *J. Atmos. Oceanic Technol.*, **14**, 143–161, https://doi.org/10.1175/1520-0426(1997)014<0143:TMWAMI>2.0.CO;2.

Lumley, J. L., and E. A. Terray, 1983: Kinematics of turbulence convected by a random wave field. *J. Phys. Oceanogr.*, **13**, 2000–2007, https://doi.org/10.1175/1520-0485(1983)013<2000:KOTCBA>2.0.CO;2.

Miller, K., and M. Rochwarger, 1972: A covariance approach to spectral moment estimation. *IEEE Trans. Inf. Theory*, **18**, 588–596, https://doi.org/10.1109/TIT.1972.1054886.

Moum, J., and J. Nash, 2009: Mixing measurements on an equatorial ocean mooring. *J. Atmos. Oceanic Technol.*, **26**, 317–336, https://doi.org/10.1175/2008JTECHO617.1.

——, M. Gregg, R. Lien, and M. Carr, 1995: Comparison of turbulence kinetic energy dissipation rate estimates from two ocean microstructure profilers. *J. Atmos. Oceanic Technol.*, **12**, 346–366, https://doi.org/10.1175/1520-0426(1995)012<0346:COTKED>2.0.CO;2.

Nasmyth, P. W., 1970: Oceanic turbulence. Ph.D. thesis, The University of British Columbia, 69 pp.

NOAA OSPO, 2019: Sea surface temperature retrievals produced by NOAA/NESDIS/STAR Office from VIIRS sensor, version 2.61. PO.DAAC, accessed 15 July 2020, https://doi.org/10.5067/GHVRS-3UO61.

Brought to you by NOAA Central Library | Unauthenticated | Downloaded 11/30/21 04:35 PM UTC

Oakey, N., 1982: Determination of the rate of dissipation of turbulent energy from simultaneous temperature and velocity shear microstructure measurements. *J. Phys. Oceanogr.*, **12**, 256–271, https://doi.org/10.1175/1520-0485(1982)012<0256:DOTROD>2.0.CO;2.

Osborn, T. R., 1980: Estimates of the local rate of vertical diffusion from dissipation measurements. *J. Phys. Oceanogr.*, **10**, 83–89, https://doi.org/10.1175/1520-0485(1980)010<0083:EOTLRO>2.0.CO;2.

——, and C. S. Cox, 1972: Oceanic fine structure. *Geophys. Fluid Dyn.*, **3**, 321–345, https://doi.org/10.1080/03091927208236085.

Perlin, A., and J. Moum, 2012: Comparison of thermal variance dissipation rates from moored and profiling instruments at the equator. *J. Atmos. Oceanic Technol.*, **29**, 1347–1362, https://doi.org/10.1175/JTECH-D-12-00019.1.

Pope, S. B., 2000: *Turbulent Flows*. 11th ed. Cambridge University Press, 771 pp.

Rusello, P. J., 2009: A practical primer for pulse coherent instruments. Nortek Tech. Rep. TN-027, 17 pp.

Saddoughi, S. G., and S. V. Veeravalli, 1994: Local isotropy in turbulent boundary layers at high Reynolds number. *J. Fluid Mech.*, **268**, 333–372, https://doi.org/10.1017/S0022112094001370.

Scully, M. E., J. H. Trowbridge, and A. W. Fisher, 2016: Observations of the transfer of energy and momentum to the oceanic surface boundary layer beneath breaking waves. *J. Phys. Oceanogr.*, **46**, 1823–1837, https://doi.org/10.1175/JPO-D-15-0165.1.

Shcherbina, A. Y., E. A. D'Asaro, and S. Nylund, 2018: Observing finescale oceanic velocity structure with an autonomous Nortek acoustic Doppler current profiler. *J. Atmos. Oceanic Technol.*, **35**, 411–427, https://doi.org/10.1175/JTECH-D-17-0108.1.

Smyth, W., and J. Moum, 2013: Marginal instability and deep cycle turbulence in the eastern equatorial Pacific Ocean. *Geophys. Res. Lett.*, **40**, 6181–6185, https://doi.org/10.1002/2013GL058403.

Sreenivasan, K. R., 1995: On the universality of the Kolmogorov constant. *Phys. Fluids*, **7**, 2778–2784, https://doi.org/10.1063/1.868656.

St. Laurent, L., and S. Merrifield, 2017: Measurements of near-surface turbulence and mixing from autonomous ocean gliders. *Oceanography*, **30** (2), 116–125, https://doi.org/10.5670/oceanog.2017.231.

Sutherland, G., G. Reverdin, L. Marié, and B. Ward, 2014: Mixed and mixing layer depths in the ocean surface boundary layer under conditions of diurnal stratification. *Geophys. Res. Lett.*, **41**, 8469–8476, https://doi.org/10.1002/2014GL061939.

Sutherland, P., and W. K. Melville, 2015: Field measurements of surface and near-surface turbulence in the presence of breaking waves. *J. Phys. Oceanogr.*, **45**, 943–965, https://doi.org/10.1175/JPO-D-14-0133.1.

Thomson, J., 2012: Wave breaking dissipation observed with SWIFT drifters. *J. Atmos. Oceanic Technol.*, **29**, 1866–1882, https://doi.org/10.1175/JTECH-D-12-00018.1.

Tong, C., and Z. Warhaft, 1995: Passive scalar dispersion and mixing in a turbulent jet. *J. Fluid Mech.*, **292**, 1–38, https://doi.org/10.1017/S0022112095001418.

Veron, F., and W. K. Melville, 1999: Pulse-to-pulse coherent Doppler measurements of waves and turbulence. *J. Atmos. Oceanic Technol.*, **16**, 1580–1597, https://doi.org/10.1175/1520-0426(1999)016<1580:PTPCDM>2.0.CO;2.

von Kármán, T., 1948: Progress in the statistical theory of turbulence. *Proc. Natl. Acad. Sci. USA*, **34**, 530–539, https://doi.org/10.1073/pnas.34.11.530.

Weller, R. A., 2015: Variability and trends in surface meteorology and air–sea fluxes at a site off northern Chile. *J. Climate*, **28**, 3004–3023, https://doi.org/10.1175/JCLI-D-14-00591.1.

Wiles, P., T. P. Rippeth, J. Simpson, and P. Hendricks, 2006: A novel technique for measuring the rate of turbulent dissipation in the marine environment. *Geophys. Res. Lett.*, **33**, L21608, https://doi.org/10.1029/2006GL027050.

Wolk, F., H. Yamazaki, L. Seuront, and R. G. Lueck, 2002: A new free-fall profiler for measuring biophysical microstructure. *J. Atmos. Oceanic Technol.*, **19**, 780–793, https://doi.org/10.1175/1520-0426(2002)019<0780:ANFFPF>2.0.CO;2.

Wyngaard, J., and O. Coté, 1971: The budgets of turbulent kinetic energy and temperature variance in the atmospheric surface layer. *J. Atmos. Sci.*, **28**, 190–201, https://doi.org/10.1175/1520-0469(1971)028<0190:TBOTKE>2.0.CO;2.

Zedel, L., A. Hay, R. Cabrera, and A. Lohrmann, 1996: Performance of a single-beam pulse-to-pulse coherent Doppler profiler. *J. Ocean. Eng.*, **21**, 290–297, https://doi.org/10.1109/48.508159.

Zhang, Y., and J. N. Moum, 2010: Inertial-convective subrange estimates of thermal variance dissipation rate from moored temperature measurements. *J. Atmos. Oceanic Technol.*, **27**, 1950–1959, https://doi.org/10.1175/2010JTECHO746.1.

Zippel, S. F., T. Maksym, M. Scully, P. Sutherland, and D. Dumont, 2020: Measurements of enhanced near-surface turbulence under windrows. *J. Phys. Oceanogr.*, **50**, 197–215, https://doi.org/10.1175/JPO-D-18-0265.1.

Brought to you by NOAA Central Library | Unauthenticated | Downloaded 11/30/21 04:35 PM UTC